Dalton Transactions

ROYAL SOCIETY OF CHEMISTRY

PERSPECTIVE

View Article Online
View Journal | View Issue

Cite this: *Dalton Trans.*, 2026, **55**, 1515

CO_2 photoreduction with heterogeneous organic photocatalysts based on π-conjugated monomers: structure–property insights and regulation strategies

Li Yang,[a] Yuqiang Sheng*[b] and Di Liu *[a]

The visible-light-driven photoreduction of CO_2 into value-added chemicals is regarded as a promising approach to alleviating the energy crisis and addressing climate change. Heterogeneous organic photocatalysts based on π-conjugated monomers, including organic polymers/organic supramolecules composed of π-conjugation units, have demonstrated significant progress in CO_2 photoreduction, attributed to their remarkable light absorption, abundant reserves of constituent elements, and tunable molecular structures. This review provides a comprehensive yet focused exploration of the general structural features of organic polymers/organic supramolecules composed of π-conjugation units, offering structure-driven design strategies tailored to address the key limitations associated with each material class in the field of CO_2 photoreduction. For the organic polymers, molecular engineering, interfacial modification, and morphological control collectively overcome key thermodynamic and kinetic bottlenecks in CO_2 photoreduction, leading to enhanced catalytic performance. Many of these approaches are equally applicable to organic supramolecules, wherein we further highlight the design of π-conjugated units that simultaneously serve as catalytic centers and defined sites for noncovalent interactions, and assembly strategies that enable control over aggregation states to construct precisely defined supramolecular architectures. Furnished with foundational knowledge and structure–property insights, this review predicts outstanding challenges. It outlines feasible research directions for heterogeneous organic photocatalysts based on π-conjugated monomers, offering an actionable design paradigm for advancing the rational development of next-generation organic photocatalysts for efficient solar-driven CO_2 conversion.

Received 13th September 2025,
Accepted 13th November 2025

DOI: 10.1039/d5dt02200b

rsc.li/dalton

1 Introduction

The increase in greenhouse gas emissions results in an increase in global temperatures, fueling extreme climate events and putting Earth's systems on the brink of irreversible damage. In this context, society has employed various approaches to control greenhouse gas emissions, among which the visible-light-driven photoreduction of CO_2 into value-added chemicals has served as a promising method to mitigate the growing energy crisis and address climate change.[1–6] However, the development of efficient photocatalytic systems remains constrained by both thermodynamic and kinetic limitations. Thermodynamically, the redox potentials and light absorption properties of photocatalysts must be simultaneously optimized to ensure sufficient driving force for CO_2 reduction. Additional challenges include the activation of inert CO_2 molecules and competing side reactions with similar reduction potentials. Kinetic limitations primarily arise from inadequate CO_2 adsorption, the temporal mismatch between ultrafast photoexcitation/charge separation processes and relatively slow surface redox reactions, coupled with sluggish kinetics of proton-coupled multi-electron pathways.[7–10]

Heterogeneous organic photocatalysts based on π-conjugated monomers are expected to serve as low-cost alternatives to inorganic semiconductors.[11–14] The use of organic π-building blocks imparts several key advantages: (i) highly conjugated units can serve directly as a photon absorber;[15] (ii) favorable transfer of charge carriers mediated by π–π stacking interactions between organic π–building blocks, as the charge reorganization energy in ordered π columns is largely reduced;[16] (iii) these organic π-building blocks can be intrinsically enriched with heteroatoms, which serve as active sites for CO_2 adsorption and subsequent catalytic conversion.[15] These π-conjugated systems fall broadly into two

[a]*School of Chemical & Environmental Engineering, China University of Mining and Technology (Beijing), Beijing, 100083, P. R. China. E-mail: liudi0713@163.com, 201849@cumtb.edu.cn*
[b]*CTBT Beijing National Data Centre and Beijing Radionuclide Laboratory, Beijing, 100085, P. R. China. E-mail: yuqiang.sheng@nrl.org.cn; Tel: (+86)10-6233-9907*

material classes: covalently bonded organic polymers composed of π-conjugation units, including linear conjugated polymers (LCPs), conjugated microporous polymers (CMPs), and specific covalent organic frameworks (COFs);[17] and organic supramolecules composed of π-conjugation units, assembled through noncovalent interactions such as hydrogen bonding or π–π stacking, exemplified by hydrogen-bonded organic frameworks (HOFs), supramolecular organic frameworks (SOFs), and related constructs.

Despite remarkable advances in material synthesis and application, the lack of a unified structure–function design framework continues to impede further breakthroughs. To address this, we present a targeted review focused exclusively on heterogeneous organic photocatalysts constructed from π-conjugated monomers. Building on the current understanding, we aim to connect the key challenges in CO_2 photoreduction to structure-driven design strategies, offering insights into the rational development of next-generation materials (Scheme 1). This review is organized around three core themes: (i) fundamentals and challenges of CO_2 photoreduction: a brief overview of the underlying photophysical and photochemical mechanisms, highlighting thermodynamic and kinetic bottlenecks. (ii) Structure-driven design strategies for heterogeneous organic photocatalysts based on π-conjugated monomers to address the key limitations in CO_2 photoreduction. For the organic polymers, emphasis is placed on molecular engineering, interfacial modulation, and morphological control to enhance charge separation and CO_2 adsorption/activation; for the organic supramolecules, the discussion is structured around two interrelated aspects: the design of π-conjugated units that simultaneously serve as catalytic centers and defined sites for noncovalent interactions and assembly strategies that enable control over aggregation states to construct precisely defined supramolecular architectures. (iii) This work proposes forward-looking research directions that target the prevailing limitations in π-conjugated-monomer-based heterogeneous organic photocatalysts for efficient solar-driven CO_2 conversion.

2 Fundamentals and challenges of CO_2 photoreduction

Photocatalytic CO_2 reductions include complex multistep processes: (1) photoexcitation upon absorption of photons with energy exceeding the semiconductor's bandgap; (2) separation and migration of the resulting electron–hole pairs to surface-active sites; (3) adsorption and activation of CO_2 on surface-active sites to form charged $*CO_2$ species; (4) subsequent reduction steps involving multiple proton-coupled electron transfer processes, C–O bond cleavage, C–H bond formation, *etc.*, leading to the generation of various intermediates and final products; and (5) desorption of the reduced products from surface-active sites.[15,18–21] Each of these steps presents distinct challenges that collectively hinder the broader applications of photocatalytic CO_2 conversion, as discussed in detail in the following sections (Scheme 1).[22–25] Notably, accurate identification of CO_2 photoreduction products remains challenging due to the similarity of reactants, products, and the catalyst itself. In this context, ^{13}C isotope labeling experiments are indispensable for unambiguously verifying the carbon source of the detected products.[26] Moreover, in systems operating without sacrificial reductants, the identification and quantification of counteroxidation products are crucial for establishing a complete and mechanistically sound photocatalytic pathway.[27]

2.1 The challenges of CO_2 photoreduction: thermodynamics

With the highest oxidation state of carbon, CO_2 shows significant thermodynamic stability attributed to its non-polar molecular structure and the high C=O bond energy (750 kJ mol^{-1}), requiring significant energy input for its activation and subsequent transformation.[28–33] Moreover, the reduction of CO_2 with H_2O to generate hydrocarbons, such as CH_4, involves a significantly higher Gibbs free energy change (818.3 kJ mol^{-1}) compared to that of water splitting into H_2 and $\frac{1}{2}O_2$ (232.2 kJ

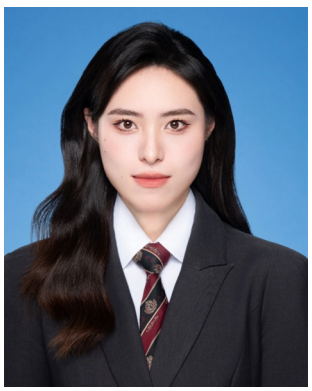

Li Yang

Li Yang is currently pursuing her Ph.D. at the School of Chemical and Environmental Engineering, China University of Mining and Technology, Beijing. Her current research focuses on the rational design of perylene diimide (PDI)-based organic semiconductor materials/different photocatalyst composites for photocatalytic reduction reactions.

Yuqiang Sheng

Yuqiang Sheng (CTBT Beijing National Data Centre and Beijing Radionuclide Laboratory) received his B.S. degree from Northwestern Polytechnical University in 2016 and Ph.D. degree from Tsinghua University in 2021. He is currently an assistant researcher at the CTBT Beijing National Data Centre and Beijing Radionuclide Laboratory. His current research is focused on the research and development of inorganic and organic materials and application in fields such as photocatalysis, gas adsorption and separation.

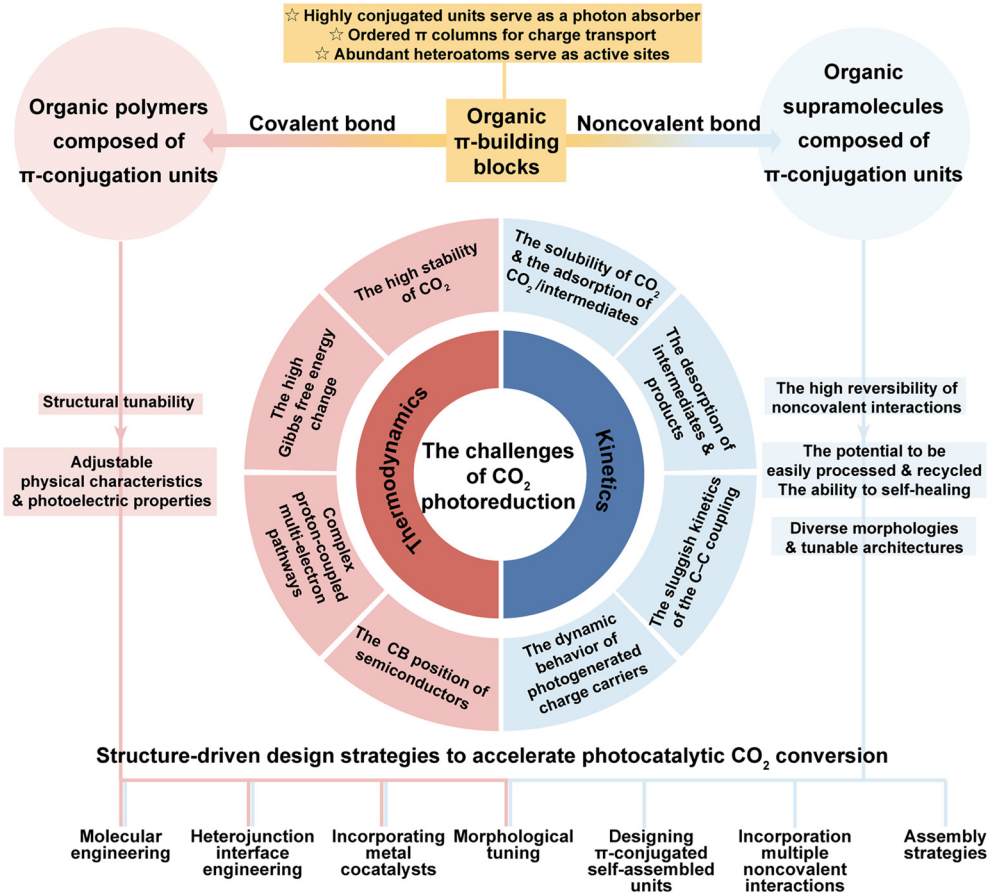

Scheme 1 Schematic illustration of structure–property insights and regulation strategies.

mol^{-1}) under standard conditions.[31] Thus, H_2 evolution is thermodynamically more favorable than CO_2 reduction in aqueous systems, making the suppression of the hydrogen evolution reaction (HER) a key challenge in selective photocatalytic CO_2 conversion.[34]

Di Liu

Di Liu (China University of Mining and Technology (Beijing)) received her B.S. degree from Shandong University in 2011 and Ph.D. degree from Tsinghua University in 2016. She is currently an associate professor in China University of Mining and Technology (Beijing). Her current research is focused on the rational synthesis and mechanism exploration of perylene diimide (PDI)-based organic semiconductor materials for visible-light-driven photocatalysis and photoelectrocatalysis.

A prerequisite for effective CO_2 photoreduction is that the photocatalyst's conduction-band edge lies at a more negative potential than the relevant CO_2 reduction redox couples (Scheme 2).[35–37] In addition, CO_2 photoreduction is inherently complex, involving multi-electron transfer processes that can yield a range of products, including carbon monoxide, methane, methanol, formic acid, and other hydrocarbons.[38–40] If a semiconductor's CB potential cannot drive the direct one-electron reduction, proton-coupled multi-electron pathways become thermodynamically preferred.[41] Likewise, the competing two-electron HER often dominates under aqueous conditions, reducing the selectivity toward CO_2 reduction products.[42,43] Consequently, balancing sufficient CB driving force with effective HER suppression remains a critical challenge in aqueous CO_2 photoreduction.

2.2 The challenges of CO_2 photoreduction: kinetics

Distinguished from thermodynamic requirements, which concern the feasibility and driving force of the overall reaction, kinetics focuses on the specific reaction pathways and rates of the reaction. However, the CO_2 photoreduction process involves multiple proton-coupled electron transfer processes, offering complex reduction routes. Therefore, efficient photocatalysts for CO_2 photoreduction must exhibit superior per-

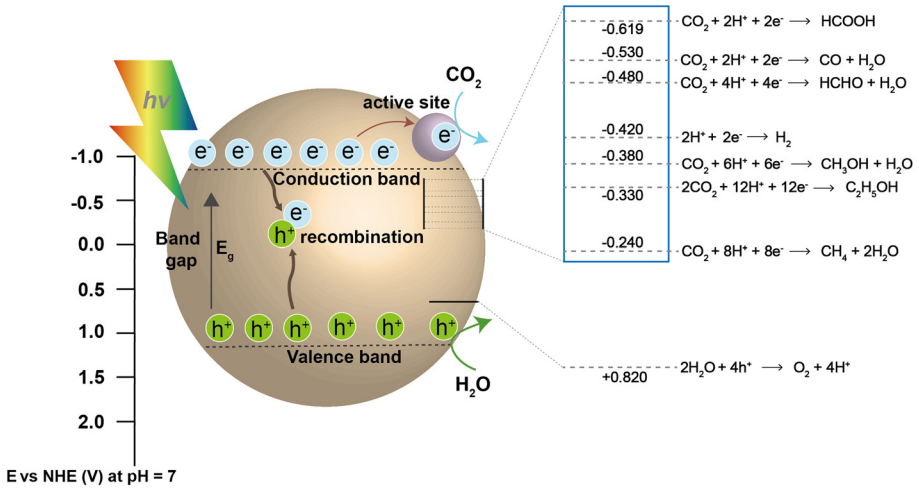

Scheme 2 Schematic illustration of the CO_2 reduction process in semiconductor-based photocatalytic systems. Adapted with permission.[44] Copyright 2023, Wiley-VCH.

formance in terms of two critical kinetic aspects: the dynamics of the CO_2 reduction reaction on the catalyst surface and the dynamic behavior of photogenerated charge carriers.[45,46]

The CO_2 reduction reaction typically proceeds through four fundamental stages: (i) adsorption of CO_2 molecules onto the photocatalyst surface; (ii) activation to form partially charged intermediates, such as $CO_2^{\bullet-}$ radical anions; (iii) C–O bond cleavage through electron–proton transfer, generating reduced intermediates; and (iv) desorption of the final products from the catalyst surface.[31] The initial step involves the adsorption of CO_2 molecules, which are typically introduced as gaseous reactants. Consequently, mass transport of gaseous CO_2 plays a critical role in the overall reaction process. However, the low solubility of CO_2 in aqueous media—only 0.033 mol L^{-1} at 25 °C and 1 atm—significantly limits its availability for surface adsorption, posing a bottleneck to reaction efficiency.[47] After initial activation, CO_2 undergoes a cascade of proton-coupled electron transfers, bond cleavages (notably C–O), and C–H bond formation. These transformations produce a wide spectrum of intermediates and final products, including C1 compounds (*e.g.*, CO, CH_4, CH_3OH, and HCOOH), C2 products (*e.g.*, CH_3COOH and C_2H_6), and even higher-order C2+ hydrocarbons.[48] However, the dynamic adsorption–desorption behavior of intermediates, combined with the inherently sluggish kinetics of C–C coupling, further limits the efficiency and selectivity of CO_2 conversion.[20]

Charge carrier dynamics also critically influence the efficiency of photocatalytic reactions, encompassing the generation of carriers upon photoexcitation, the diffusion and recombination of photogenerated electron–hole pairs, and subsequent transfer to catalytically active sites for CO_2 reduction (Scheme 3). Therefore, close attention to the dynamics of photogenerated carriers is essential for improving overall photocatalytic performance. Upon photoexcitation, excitons are generated within femtoseconds (fs) and rapidly dissociate into free electrons and holes, which then relax to

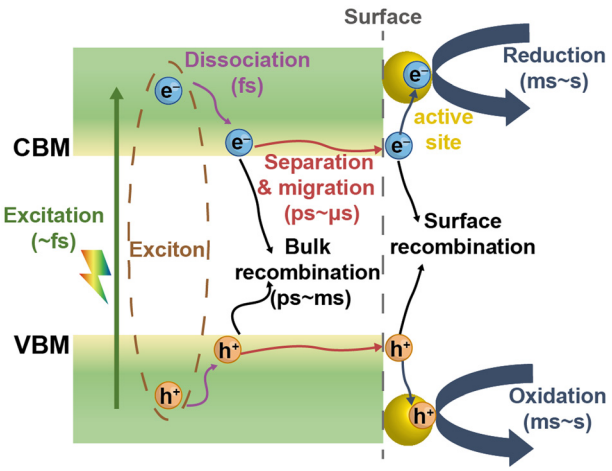

Scheme 3 Dynamics of photogenerated electrons and holes in a single photocatalyst.

the conduction band minimum (CBM) and valence band maximum (VBM), respectively. These photogenerated carriers follow two competing pathways: (i) migration to the semiconductor–solution interface, where they participate in surface redox reactions, or (ii) recombination within the bulk or at surface trap states. Only electrons that successfully reach catalytically active sites can drive CO_2 reduction.[49] However, because the timescale for carrier migration and surface reaction (typically ms to s) is orders of magnitude longer than that of charge recombination (ns or less), most photogenerated carriers undergo recombination before they can reach the surface to participate in catalytic reactions.[50] This spatiotemporal mismatch severely limits the quantum efficiency of photocatalysts. Therefore, improving charge separation and transport remains a central challenge. A comprehensive understanding of carrier generation, relaxation, migration, and recombination—across

both temporal and spatial dimensions—is essential for overcoming current limitations and enhancing CO_2 photoreduction performance.

In summary, major bottlenecks in CO_2 photoreduction remain centered on inefficient charge carrier separation and transport, as well as the sluggish surface activation and conversion of CO_2. Addressing these challenges necessitates continued advances in the rational design of heterogeneous organic photocatalysts based on π-conjugated monomers, thereby contributing to the development of scalable and cost-effective CO_2 reduction technologies.

3 Design strategies of organic polymers composed of π-conjugation units for CO_2 photoreduction

Organic polymers composed of π-conjugation units, including LCPs, CMPs, and specific COFs, are composed of diverse organic π-building blocks.[17] Structurally, the organic polymers comprise two main components: a conjugated backbone and flexible side chains.[51] In the organic polymers, the backbone typically consists of sequences of sp^2-hybridized carbon atoms together with heteroatoms. The conjugated backbone is the dominant factor in dictating the electronic properties, specifically the energy levels and bandgaps.[52] Through σ-bonds, the sp^2-hybridized carbons construct the supporting backbone, while the remaining p_z wave functions—orthogonal to the backbone—combine to form π-bonds, which provide the basis for the semiconducting or conducting properties. Because σ-bonds do not directly contribute to charge transport, discussions of electronic properties generally focus on the π-bands.[11] π-Electron delocalization along the backbone, resulting from p_z orbital overlap, provides a 'highway' for charge mobility;[53] by extending the conjugation, the electron density spreads over a larger region, enhancing delocalization and reducing the energy gap between the lowest unoccupied molecular orbital (LUMO) and the highest occupied molecular orbital (HOMO).[54,55]

The structural tunability afforded by organic synthesis enables extensive optimization and programmability of both the electronic and physical properties of these materials. Consequently, key physical characteristics—such as solubility—as well as optoelectronic properties—such as charge transport and light absorption—can be tailored through rational molecular design and structural modification.[11] In addition to molecular-level design, morphological factors play a critical role in tuning catalytic performance. Their high surface area and tunable pore environments facilitate efficient CO_2 mass transfer, charge transfer, and accessibility to active sites.[15] These unique properties make organic polymers composed of π-conjugation units attractive candidates for photocatalytic CO_2 reduction, as summarized in Table 1. Notably, the reported CO_2 photoreduction rates are sensitive to experimental parameters, including the light source spectrum, optical filters, light intensity at the sample surface, choice and loading of co-catalysts, type and concentration of sacrificial agents, sample concentration, and reactor headspace pressure.[56] To ensure meaningful comparisons, it has been widely recommended that apparent quantum yields (AQYs) be reported alongside gas evolution rates. Furthermore, the influence of catalyst loading warrants careful evaluation: insufficient catalyst dosage can limit light absorption and photon utilization, whereas excessive loading may induce light scattering and reduce the accessibility of active sites, ultimately compromising overall efficiency.

A representative example is the triazine-based polymer backbone, one of the most widely studied frameworks in this field. The triazine ring, featuring three C=N moieties, can theoretically accommodate up to three electrons, enabling it to function as an efficient electron-storage unit,[61] making it a highly effective active site for CO_2 reduction.[62,63] In addition, the nitrogen-rich composition of triazine provides abundant Lewis basic sites, which facilitate strong CO_2 adsorption and activation—key prerequisites for efficient catalytic conversion.[64]

For instance, Gao *et al.*[57] designed a triazine-based COF membrane that integrates robust light-harvesting units, efficient catalytic centers, and a membrane architecture optimized for rapid charge and mass transport (Fig. 1a). This biomimetic design achieved a record CO yield of 1240 μmol g^{-1} over 4 hours, with nearly 100% selectivity and exceptional stability sustained over 16 cycles. Within this system, triazine units act as electron reservoirs, imide moieties serve as catalytic centers, and the continuous membrane structure facilitates efficient carrier and reactant diffusion—together accounting for the system's outstanding CO_2-to-CO performance. The triazine ring is rarely used to create photocatalytically active porous LCPs due to limited synthetic methodologies. In this regard, Zhu *et al.*[58] developed a series of porous methylated triazine-based linear conjugated polymers (Fig. 1b). These materials delivered high CO evolution rates (218.9 μmol g^{-1} h^{-1}) with quantitative selectivity and concurrent water oxidation. The polymers were synthesized *via* a simple condensation of benzamidine and acetic anhydride, yielding abundant methylated triazine units. By modulating the length of electron-rich benzyl linkers within the polymer backbone, the authors tuned both optical absorption and exciton dissociation dynamics, thereby promoting efficient photoinduced charge separation and transport. Additionally, the spatial alignment of electron-rich sites and CO_2 adsorption sites is pivotal for optimizing the photocatalytic process. Zhou *et al.*[59] reported a porphyrin–triazine COF featuring strongly electron-withdrawing triazine cores and ether linkages (Fig. 1c). This framework spatially aligned electron-rich domains with CO_2 adsorption sites, significantly enhancing reduction efficiency. The introduction of ether groups further improved charge separation and enabled electron accumulation at the C=N imine linkages—contributing to superior overall catalytic activity.

In addition to triazine-based polymers, various novel organic polymers have been developed for CO_2 photoreduc-

Table 1 Organic polymers composed of π-conjugation units for photocatalytic CO_2 reduction

Photocatalyst	Catalyst dosage	Reaction medium	Light source	Rate max. [μmol g^{-1} h^{-1}]	Selectivity [%]	Stability [h]	AQY/ AQE [%]	Isotope-labeling experiments	Oxidation products [μmol g^{-1} h^{-1}]	Ref.
ImI-CMP@Co	10 mg	MeCN/TEOA (4 : 1, v/v), $[Ru(bpy)_3]Cl_2$	300 W Xe lamp (λ > 420 nm)	CO, 2953	—	2.3	0.52	YES	—	65
pTA-Ph	2 mg	Gas–solid regime, CO_2/H_2 (1 : 3, at 1.15 bar)	300 W Xe lamp (350–800 nm)	CO, 9.5	98	100	0.088	YES	—	66
OXD-TPA	5 mg	Gas–solid regime, H_2O vapor	300 W Xe lamp (λ > 420 nm)	CO, 37.15	100	20	0.19	YES	O_2	67
CPs-BT	15 mg	H_2O/CH_3CN /TEOA	300 W Xe lamp (λ > 420 nm)	CO, 18.2 μmol h^{-1}	81.6	24	1.75	YES	—	68
CLP-CS	10 mg	MeCN/H_2O/TEOA, $[Co(bpy)3]^{2+}$	300 W Xe lamp	CO, 16.13 μmol h^{-1}	90	15	—	YES	—	69
CoPcPDA-CMP NSs	2 mg	Gas–solid regime, H_2O vapor	300 W Xe lamp (420 nm < λ < 800 nm)	CO, 14.27	92	20	—	YES	O_2	70
BP-T-LCP	5 mg	Gas–solid regime, H_2O vapor	300 W Xe lamp (λ > 420 nm)	CO, 218.9	100	20	1.01	YES	O_2, 107.1	58
PP-COF-Co	2 mg	MeCN/H_2O (2 : 3, v/v); BIH and $Ru(bpy)_3Cl_2{\cdot}6H_2O$	10 W LED lamp ($\lambda \geq$ 400 nm)	CO, 7580	91.5	20	—	YES	—	71
TOT-TAPP	20 mg	H_2O/TEOA (1 : 1, v/v)	300 W Xe lamp (800 > λ > 200 nm)	CO, 34.8	—	15	—	—	—	59
Co/Ni-Btt-Bpy COF	1 mg	MeCN/H_2O (2 : 1, v/v); 0.5 M triisopropanolamine and 0.6 × 10^{-3} M $[Ru(bpy)_3]Cl_2$	10 W LED lamp (λ = 420 nm)	CO, 9800	94.3	20	1.1	YES	—	4
Cu_3-BPY-COF(Ru/Co)-2	2.0 mg	ACN/H_2O/TEOA (3 : 1 : 1, v/v/v)	300 W Xe lamp (λ > 420 nm)	CH_4, 31.5	95	15	—	YES	—	72
PFT	1 mg	MeCN/TEOA	Xenon lamp with 100 mW cm^{-2} (AM 1.5 filter)	CO, 279	88	12	0.115	YES	—	73
Tx–TzTz–CMP-2	2.0 mg	MeCN/H_2O (1/3, v/v)	White LED lamp (λ > 420 nm)	CH_4, 300.6	71.2	11.7	0.025	YES	—	74
Bi-TTCOF-Zn	100 mg	H_2O	300 W Xe lamp (420–800 nm)	CO, 11.56	100	24	—	YES	CO/O_2, 2 : 1	75
BtE-COF	10 mg	MeCN/TEOA/H_2O (6 : 2 : 2, v/v/v)	300 W Xe lamp (λ > 420 nm)	CO, 725	88	16	—	YES	—	76
2N-COF	1 mg	H_2O	300 W Xe lamp	CO, 310	100	64	0.36	YES	O_2	57
P-2CN	10 mg	MeCN/H_2O/TEOA (4 : 1 : 1, v/v/v); 0.1 mmol 2,2-bipyridine	300 W Xe lamp (λ > 420 nm)	CO, 3200	61.5	30	4.6	YES	—	77
viCOF-bpy-Re	10 mg	H_2O	300 W Xe lamp (λ > 420 nm)	CO, 190.6	100	50	1.08	YES	O_2, 90.2	78
PFBT Pdots	50 μg mL^{-1}	0.2 M TEOA	LED light (420–750 nm)	CO, 57	100	25	—	YES	—	79
Fe SAS/Tr-COF	5 mg (optimal)	MeCN/H_2O/TEOA (3 : 1 : 1, v/v/v)	300 W Xe light (420–750 nm)	CO, 980.3	96.4	20	3.17	YES	—	80
TCOF-$MnMo_6$	40 mg (optimal)	Gas–solid regime, H_2O	300 W Xe lamp (400–800 nm)	CO, 37.25	100	20	0.0067	YES	O_2	81
TPA-PQ	1 mg	MeCN/H_2O (2 : 1, v/v)	300 W Xe light (400–800 nm)	CH_4, 2021.5	97	60	0.1	YES	—	82
COF-318-TiO_2	2 mg	Gas–solid regime, H_2O vapor	Simulated sunlight irradiation (λ = 380–800 nm)	CO, 69.67	—	20	—	YES	O_2	83
N-CP-D	5 mg	MeCN/H_2O (7 : 3, v/v), TEOA, Co(II) bipyridine complexes cocatalyst	300 W Xe lamp (λ > 420 nm)	CO, 2247	82	25	1.23	YES	—	60
CT-COF	50 mg	Gas–solid regime, H_2O	300 W Xe lamp (λ > 420 nm)	CO, 102.7	98	9	0.104	YES	O_2, 51.3	84

Table 1 *(Contd.)*

Photocatalyst	Catalyst dosage	Reaction medium	Light source	Rate max. [μmol g^{-1} h^{-1}]	Selectivity [%]	Stability [h]	AQY/ AQE [%]	Isotope-labeling experiments	Oxidation products [μmol g^{-1} h^{-1}]	Ref.
COF-367-Co	5 mg	MeCN/H_2O/TEOA	λ > 420 nm	HCOOH, 93.0	97.1	8	—	YES	—	85
PI-COF	10 mg	MeCN/H_2O/TEOA (3 : 1 : 1, v/v/v), $[Ni(bpy)_3]^{2+}$	300 W Xe lamp (λ > 420 nm)	CO, 483.0	93	20	0.55	YES	—	86
Ni-TpBpy	10 mg (optimal)	MeCN/H_2O/TEOA (3 : 1 : 1, v/v/v), 2,2′-bipyridine, $[Ru(bpy)_3]Cl_2{\cdot}6H_2O$	300 W Xe lamp (λ > 420 nm)	CO, 966	96	15	0.3	YES	—	87
PEosinY-1	10 mg	Gas–solid regime, H_2O vapor	300 W Xe lamp (λ > 420 nm)	CO, 33	92	50	—	YES	—	88
TTCOF-Zn	10 mg (optimal)	H_2O	300 W Xe lamp (λ = 420–800 nm)	CO, 2.06	100	60	—	YES	CO/O_2, 2 : 1	89
COF-367-Co NSs	5 mg	0.1 M $KHCO_3$, $[Ru(bpy)_3]Cl_2{\cdot}6H_2O$, AA	300 W Xe lamp (λ > 420 nm)	CO, 10 162	78	12	—	YES	—	90
Zn-TPA-BPy-1	1 mg	TEOA, $[Ru(bpy)_3]Cl_2{\cdot}6H_2O$	60 W LED lamp	CH_4, 753.2	89.7	13.3	3.45	YES	—	91
SCTF/$ZnIn_2S_4$	10 mg	MeCN/H_2O, furfuryl alcohol	AM 1.5G	CO, 43.9	95	30	1.86	YES	Furfural	92
$In_{2.77}S_4$(P6)	3 mg	H_2O	450 W Xe lamp	C_2H_4, 67.65	98.9	10	5.1	YES	O_2	93
RuRu′/Ag/P10	4 mg	DMA/TEOA (4 : 1, v/v)	300 W Xe lamp (λ > 420 nm)	HCOOH, 3350	96	140	11.2	YES	—	94
DA-CTF@DPT-Co	2 mg	MeCN/H_2O/TEOA (9 : 1 : 1, v/v/v)	300 W Xe lamp ($\lambda \geq$ 420 nm)	CO, 724	92	25	0.94	YES	—	95
ZnPor-RuCuDAC	8 mg	MeCN/H_2O/TEOA (12 : 2 : 1, v/v/v)	150 W Xe lamp	Acetate, 400.5	95.1	40	—	YES	—	96
$[Cz_2\text{-}DbtO_3\text{-}Ru_1]_n$	2 mg	MeCN/TEOA (4 : 1, v/v)	LED lamp (400 nm < λ < 700 nm)	HCOOH, 15 716.7	95	15	9.0	YES	—	97
TPy-COF-Co	1 mg (optimal)	MeCN/H_2O/TEOA (4 : 1 : 1, v/v/v), $[Ru(bpy)_3]Cl_2{\cdot}6H_2O$	300 W Xe lamp ($\lambda \geq$ 420 nm)	CO, 138 750 H_2, 104 430	Tunable syngas	16	2.14	YES	—	98
CuPor-POP-Mo	5 mg (optimal)	MeCN/H_2O/TEOA (29.5 : 0.5 : 6, v/v/v), $[Ru(bpy)_3]Cl_2{\cdot}6H_2O$	300 W Xe lamp (420–780 nm)	C_2H_6, 472.5	87.5	16	0.55	YES	—	99
PAF-332-DCM	5 mg	Gas–solid regime, H_2O	300 W Xe lamp (λ > 400 nm)	CO, 344.1	—	30	0.127	YES	—	100
Co-PyPDA-COF	1 mg	MeCN/H_2O (13 : 5, v/v), $[Ru(bpy)_3]Cl_2{\cdot}6H_2O$	300 W Xe lamp (λ > 420 nm)	CO, 30.5	95.8	16		YES	—	101

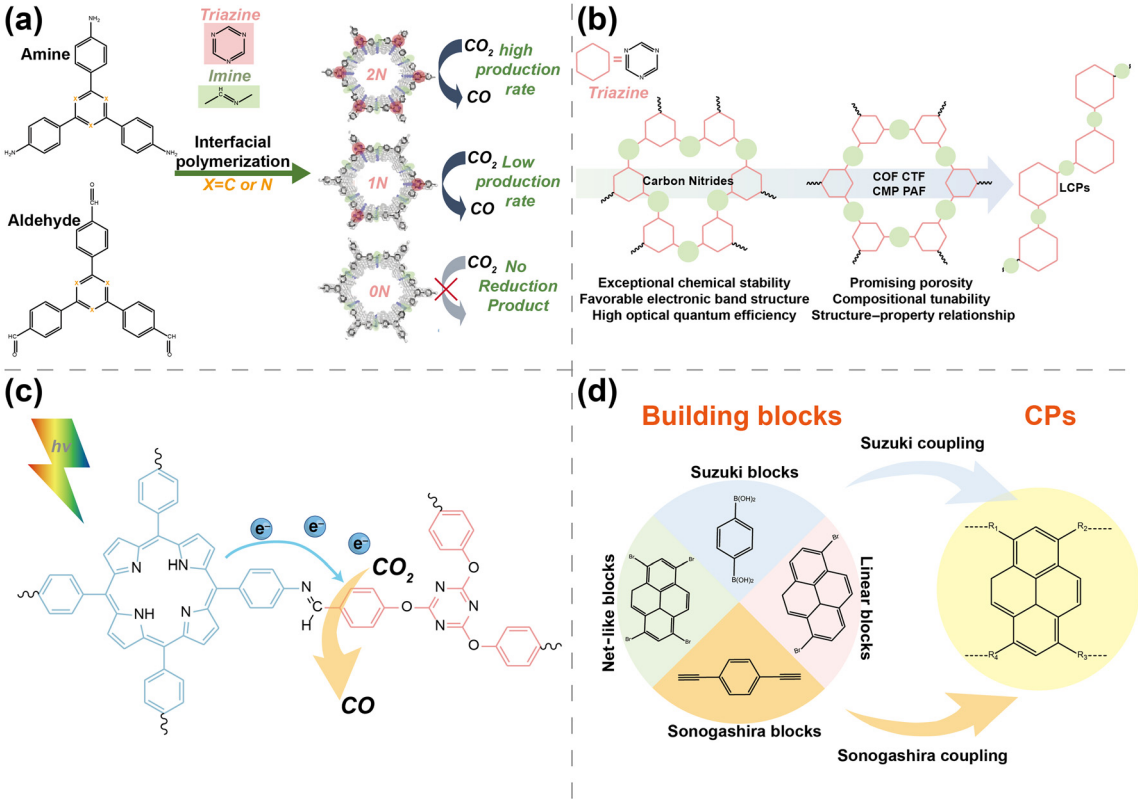

Fig. 1 (a) Schematic illustration of the synthesis of 0N-COF, 1N-COF and 2N-COF membranes. Adapted with permission.[57] Copyright 2023, American Chemical Society. (b) Illustration of the development of triazine-based conjugated polymers (CPs) for photocatalysis. Adapted with permission.[58] Copyright 2025, Wiley-VCH. (c) Charge transfer mechanisms of photocatalytic CO_2 reduction on TOT-TAPP COFs. Adapted with permission.[59] Copyright 2025, Wiley-VCH. (d) Illustration of synthesis and the strategy of eliminating the charge-transfer bridge. Adapted with permission.[60] Copyright 2020, Springer Nature.

tion. Wang *et al.*[60] reported four types of pyrene-based CPs, featuring either alkynyl or non-alkynyl linkages (Fig. 1d). In conjugated polymers incorporating alkynyl units, photoexcited electrons are generated and efficiently transferred along the polymer backbone *via* the conjugated alkynyl bridges. However, the extended delocalization of electrons throughout the framework reduces their accessibility to cocatalysts, as the subsequent transfer relies primarily on weak intermolecular π–π interactions. In contrast, conjugated polymers lacking alkynyl bridges suppress intramolecular charge delocalization, thereby localizing photoexcited electrons and facilitating their more efficient delivery to active sites through intermolecular cascade channels. The optimized polymer, net-like directly connected CPs without alkynyl groups, exhibited an impressive CO evolution rate of 2247 μmol g^{-1} h^{-1}—a 138-fold increase over that of their unmodified counterpart, net-like alkynyl-connected CPs.

Despite recent progress, the photocatalytic efficiency of organic polymers remains constrained by multiple factors, of which sluggish charge separation and transport constitute a crucial limitation.[102,103] These processes are governed by both bulk (intra-chain or intra-framework) and interfacial charge transfer dynamics. To address these limitations, several strategies have been developed. For instance, the incorporation of donor–acceptor (D–A) architectures within organic polymer backbones has been shown to enhance bulk charge separation by inducing a strong dipole moment. Additionally, surface engineering—such as anchoring electron acceptors onto the organic polymer surfaces or constructing semiconductor heterojunctions—can significantly improve interfacial charge transfer.[77]

Beyond charge dynamics, the adsorption and activation of CO_2 at the catalyst surface remain persistent challenges that limit overall conversion efficiency. To overcome these bottlenecks, strategies such as increasing the specific surface area and incorporating metal cocatalysts have been explored to enhance CO_2 adsorption and activation. These approaches, along with their mechanistic implications, will be discussed in detail in the following sections.[104]

3.1 Building D–A type organic polymers composed of π-conjugation units

The limited charge separation efficiency in organic polymers composed of π-conjugation units stems from the absence of a sufficient internal driving force, which impedes carrier separation and transport. To address this kinetic constraint, D–A engineering refers to the construction of polymer backbones with electron-donating and -withdrawing units integrated. The

resulting intramolecular push–pull interactions between electron-rich donor and electron-deficient acceptor units facilitate exciton dissociation and promote directional charge migration toward cocatalyst interfaces or substrate molecules, thereby enhancing photocatalytic efficiency (Scheme 4).[77,82] The D–A arrangement within the frameworks induced a redistribution of the HOMO and LUMO between the electron donor and acceptor units, resulting in newly formed frontier molecular orbitals. This reorganization effectively modulated the energy bandgap, thereby extending the material's light absorption range.[17] Therefore, adjusting the structure and ratio of donor and acceptor units enables precise control over the band structure and optoelectronic properties, ensuring alignment with the redox requirements of specific CO_2 reduction pathways.[17,105] Thus, D–A-type organic polymers provide a molecular-level strategy for simultaneously promoting carrier separation and regulating the electronic structure, thereby addressing both kinetic and thermodynamic limitations.

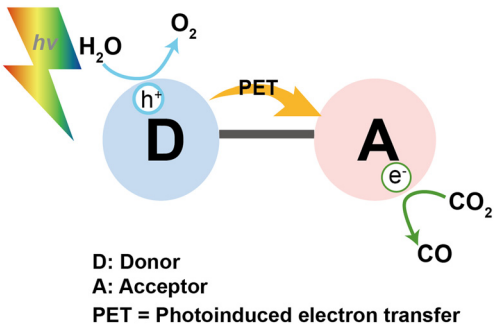

Scheme 4 Schematic illustration of an intramolecular D–A system.

The carbazole moiety is known for its electron-rich character and excellent hole-transporting capability, whereas triazine-based units exhibit high electron affinity and consequently enable efficient electron drift mobility.[106] In this context, Lei *et al.*[84] developed a D–A COF (CT-COF) *via* Schiff base condensation between carbazole- and triazine-based monomers (Fig. 2a). The resulting material exhibits a well-aligned energy band structure, strong visible-light absorption, and a high

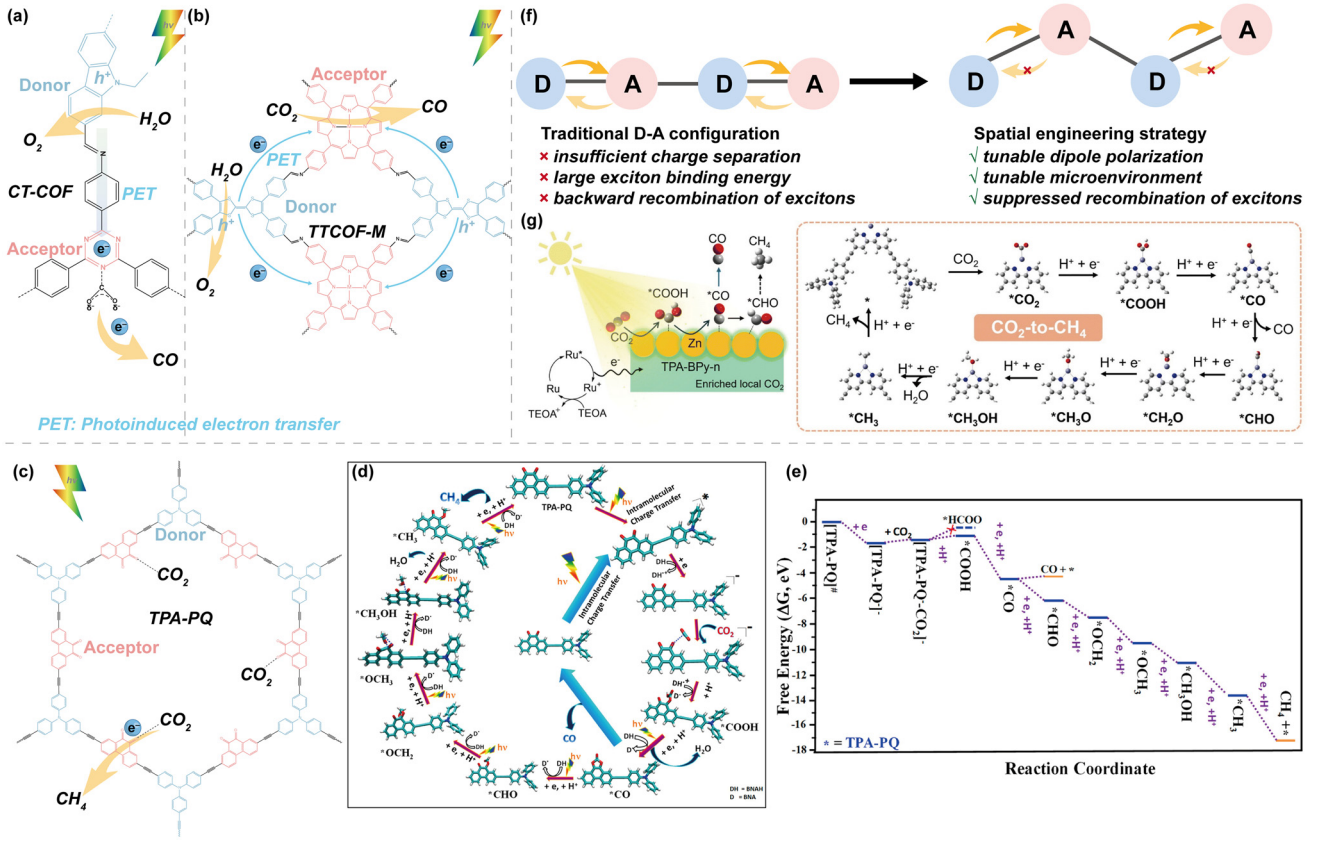

Fig. 2 Schematic illustration of visible-light-driven CO_2 reduction involving (a) the CT-COF. Adapted with permission.[84] Copyright 2020, Wiley-VCH. (b) TTCOF-M. Adapted with permission.[89] Copyright 2019, Wiley-VCH and (c) TPA-PQ. Adapted with permission.[82] Copyright 2021, American Chemical Society. (d) Gibbs free energy pathway for the formation of CH_4 *via* CO from CO_2. Adapted with permission.[82] Copyright 2021, American Chemical Society. (e) Plausible catalytic cycle comprising the different reaction intermediates. Adapted with permission.[82] Copyright 2021, American Chemical Society. (f) Comparison with the traditional D–A configuration and the design strategy for spatial engineering. Adapted with permission.[91] Copyright 2025, The Royal Society of Chemistry. (g) Schematic illustration showing the possible reaction pathway for photocatalytic CO_2 reduction on Zn-TPA-BPy-*n*.[91] Adapted with permission.[91] Copyright 2025, The Royal Society of Chemistry.

density of nitrogen sites. The D–A framework facilitates efficient exciton dissociation and charge transport, enabling the CT-COF to drive both CO_2 reduction and water oxidation without the assistance of external co-catalysts. This system achieves a CO evolution rate of 102.7 μmol g^{-1} h^{-1}, accompanied by near-stoichiometric O_2 generation, highlighting its potential as a complete artificial photosynthetic platform.

In another example, electron-deficient metalloporphyrin (TAPP) complexes are well-known for their strong visible-light absorption and potential in CO_2 photoreduction, while electron-rich tetrathiafulvalene (TTF) has proven to be an excellent electron donor due to its rapid electron-transfer capabilities. Based on these features, Lu *et al.*[89] designed a series of crystalline two-dimensional (2D) COFs (TTCOF-M, where M = 2H, Zn, Ni, or Cu) based on the combination of TTF and TAPP units (Fig. 2b). Within the framework, covalent bonding ensures efficient electron transfer from TTF to TAPP, resulting in spatially separated electrons and holes for CO_2 reduction and H_2O oxidation, respectively. Among these, TTCOF-Zn exhibited the highest activity, producing 2.06 μmol g^{-1} h^{-1} of CO with nearly 100% selectivity and simultaneous O_2 evolution. Mechanistic studies suggest that under visible-light irradiation, the TTF unit (serving as the HOMO center) absorbs photons and donates electrons to the TAPP unit (LUMO center). The electrons are subsequently transferred to the catalytic metal centers (Zn or Cu) within TAPP to drive CO_2 reduction, while the remaining holes in TTF oxidize water molecules to release O_2. This dual-function system maintains charge neutrality by continuously extracting electrons from water, thereby sustaining the overall photoredox cycle.

The selective photocatalytic reduction of CO_2 to CH_4 remains a considerable challenge, as it involves an eight-electron, multi-proton transfer process that is kinetically more demanding than the two-electron reduction to CO. Barman *et al.*[82] developed D–A CMP (TPA-PQ) by integrating an electron donor (tris(4-ethynylphenyl)amine, TPA) and an acceptor (phenanthraquinone, PQ) (Fig. 2c–e). This architecture enables efficient intramolecular charge transfer (ICT) under visible-light irradiation, driving selective CO_2-to-CH_4 conversion with a remarkable yield of 32.2 mmol g^{-1} and a production rate of 2.15 mmol g^{-1} h^{-1}, while maintaining selectivity above 97%. The adjacent keto groups in the PQ unit were shown to play a pivotal role in lowering the reduction barrier and stabilizing CO_2 adsorption intermediates, thereby enhancing photocatalytic performance. Meanwhile, the vital role of ICT in advancing photocatalysis is further demonstrated by the synthesis of another CMP (TEB-PQ) that lacks D–A capability, where the donor group TPA is replaced with triethynylbenzene (TEB); TEB-PQ shows about eight times lower activity for CO_2-to-CH_4 photoreduction compared to TPA-PQ.

Notably, conventional two-component D–A systems with π-conjugated frameworks often exhibit rapid backward charge recombination in the lateral direction.[107] To overcome this limitation, modification strategies have been developed to reconstruct and optimize the structures of D–A type organic polymers. A common approach involves introducing acetylene linkers or aromatic spacers to form a D–π–A configuration, thereby extending π-conjugation and modulating the intramolecular charge distribution. The incorporation of π-bridges not only facilitates directional charge transfer and suppresses back recombination but also extends charge carrier diffusion lengths and enhances electron–hole separation stability.[108] Meng *et al.*[74] synthesized two redox-active, truxene-based CMP incorporating thiazolo[5,4-*d*]thiazole linkages for metal-free photocatalytic CH_4 production. Among them, Tx–TzTz–CMP-2 with an extended π-conjugated system using phenyl as a π-bridge exhibited a CH_4 generation rate of 300.6 μmol g^{-1} h^{-1} with 71.2% selectivity, without the need for metal cocatalysts or photosensitizers. In addition, the nitrogen site on the thiazole unit served as both an electron reservoir and a catalytic center, facilitating CO_2 activation and subsequent hydrogenation to CH_4. Recently, Lan *et al.*[91] synthesized a series of regioisomeric alkynyl-linked CMPs (TPA-BPy-*n* (*n* = 1, 2, 3)), by precisely controlling the regiochemistry of bipyridine substituents in modular tris(4-ethynylphenyl)amine precursors. Atomically dispersed Zn centers were coordinated within the bipyridine units to catalyze CO_2 photoreduction. Among these, Zn-TPA-BPy-1 achieved the highest performance, with a CH_4 production rate of 753.2 μmol g^{-1} h^{-1} and a selectivity of 89.7%. The incorporation of D–π–A motifs with pronounced intramolecular charge transfer enabled systematic control of framework dipole moments, while the spatial orientation determined whether metal coordination occurred inside or outside the channels. Mechanistic investigations reveal that the synergistic interaction between Zn sites and the TPA-BPy-1 framework lowers the energy barriers for *COOH and *CO intermediate formation, and thermodynamically favors the generation of *CHO species, thereby driving the selective photoreduction of CO_2 to CH_4 (Fig. 2f and g).

Building hetero-motif molecular junction (HMMJ) structures. To further expand the structural versatility and functional integration of D–A systems, recent studies have explored more complex architectures that go beyond simple D–A pairings (Scheme 5). One such approach involves the construction of hetero-motif molecular junctions (HMMJs)—periodically distributed molecular junctions that integrate multiple functional motifs into a single, spatially ordered framework.[109,110]

Inspired by the design concept of heterojunctions, Lan *et al.*[111] pioneered the development of HMMJ photocatalysts. These materials are composed of precisely defined photosensitive, oxidative, and reductive motifs that are assembled through direct bonding, grafting, or post-synthetic modification. The highly tunable arrangement of these molecular components allows precise regulation of band structures and charge transfer pathways within the photocatalyst.[105] Crucially, the rational selection and spatial alignment of oxidation and reduction motifs are essential for achieving directional charge separation and efficient photoredox activity.

For instance, Li *et al.*[75] designed a series of redox-active molecular junction COFs (M-TTCOF-Zn, where M = Bi, Tri, Tetra) by covalently linking TAPP-Zn units—serving as CO_2 reduction centers—with multidentate tetrathiafulvalene (TTF)

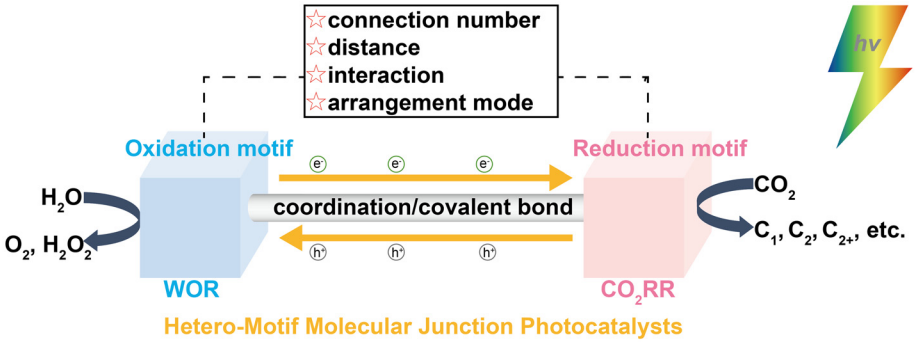

Scheme 5 Design ideas for screening the appropriate structural motifs to construct hetero-motif molecular junction photocatalysts as well as a schematic representation of artificial photosynthesis. Adapted with permission.[109] Copyright 2024, American Chemical Society.

units as water oxidation centers (Fig. 3a). The covalent linkage between TAPP-Zn and multidentate TTF facilitates directional electron transfer from TTF to TAPP-Zn, enabling spatial separation of photoinduced charge carriers: photoexcited electrons localize on TAPP-Zn for CO_2 reduction, while photogenerated holes accumulate on TTF units for water oxidation. Among the series, Bi-TTCOF-Zn exhibited the highest activity, achieving a CO evolution rate of 11.56 μmol g^{-1} h^{-1} with nearly 100% selectivity.

In another advancement, Lu *et al.*[81] proposed a general strategy for integrating polyoxometalate (POM) single clusters into the nanopores of crystalline COFs through covalent confinement (Fig. 3b). The resulting COF–POM hybrid materials combine light-harvesting, charge transfer, and catalytic functions within a unified framework. Among these, TCOF-$MnMo_6$ achieved the highest CO generation rate of 37.25 μmol g^{-1} h^{-1} with near-complete selectivity under gas–solid phase conditions. Mechanistic analysis revealed that photoinduced electron transfer (PET) occurs from the COF backbone to the embedded POM cluster, where CO_2 reduction is catalyzed by the POM and water oxidation is driven by the COF. Covalent anchoring at the molecular level ensures strong interfacial electronic coupling, significantly enhancing charge-transfer efficiency.

In summary, D–A-type organic polymers and their advanced hetero-motif architectures represent a promising class of materials for CO_2 photoreduction. Their modular design enables precise tuning of optoelectronic properties, promotes directional charge transport, and allows the incorporation of diverse catalytic functionalities, which are essential for

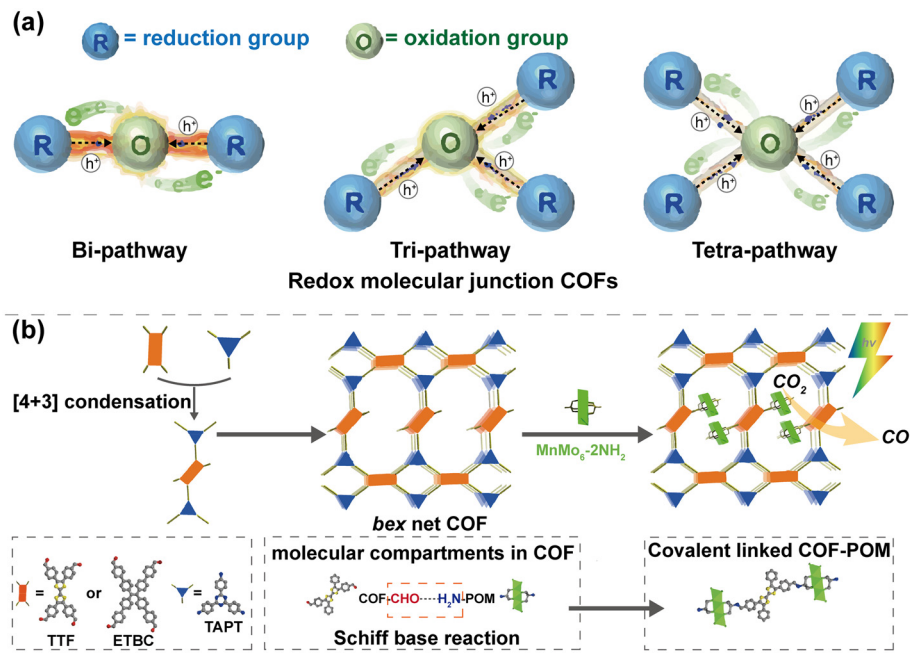

Fig. 3 (a) Redox molecular junction COFs with possible connection modes. Adapted with permission.[75] Copyright 2023, American Chemical Society. (b) Schematic representation of uniformly dispersed POM clusters in the COF by confining them into the pores of the COF through covalent linkages. Adapted with permission.[81] Copyright 2022, American Chemical Society.

efficient CO_2 conversion. Nevertheless, the assembly of D and A components remains challenging due to their multiple interacting sites, usually resulting in unpredictable structural outcomes. Moreover, most reported D–A-type organic polymers exhibit AA stacking, which confines charge and energy transport to intralayer through-bond or channel-restricted pathways. The development of architectures that combine intralayer through-bond transport with interlayer through-space π–π interactions to facilitate multidimensional charge and energy transport remains insufficiently explored.[112]

3.2 Building semiconductor heterojunctions

While molecular-level D–A engineering has shown remarkable promise, constructing heterojunctions between distinct semiconducting components offers another powerful strategy for enhancing interfacial charge transfer and preserving redox potentials in photocatalytic systems. A heterojunction is the interface between two semiconductors with distinct energy band structures. Based on the alignment of these bands and the mechanisms of photogenerated charge transfer, heterojunction photocatalysts are generally categorized into several types, among which type II,[113–115] Z-scheme,[116–119] and S-scheme heterojunctions[120–123] are the most extensively studied.[105] Unlike the unidirectional charge migration observed in type II heterojunctions, the Z-scheme and S-scheme facilitate spatial separation of charge carriers by retaining electrons in the more negative CB and holes in the more positive VB.[124,125] This configuration improves charge separation efficiency and preserves the strong redox potentials necessary for high-performance photocatalysis.[126] The following sections will focus on recent advances in Z-scheme and S-scheme heterojunctions, highlighting their design principles, charge-transfer mechanisms, and applications in CO_2 reduction (Scheme 6).

Recent studies have demonstrated that rational design of Z-scheme heterojunctions—particularly those integrating organic and inorganic components—can effectively enhance charge separation and preserve redox potentials in CO_2 photoreduction systems. For instance, Zhi *et al.*[127] developed 2D imide-based covalent organic polymer nanosheets (CoPcPDA-CMP NSs) as a Z-scheme artificial photosynthetic platform for overall CO_2 reduction. These nanosheets feature cobalt phthalocyanine (CoPc) units as reduction sites and 3,4,9,10-perylenetetracarboxylic diimide (PDI) moieties as oxidation sites. Under visible-light irradiation and using water as the sacrificial electron donor, CoPcPDA-CMP NSs achieved a CO evolution rate of 14.27 μmol g^{-1} h^{-1} with a selectivity of 92%, highlighting their potential for integrated solar-driven redox catalysis.

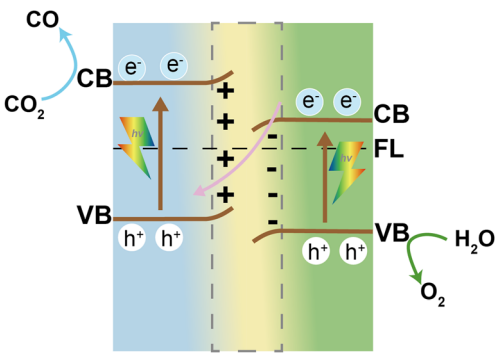

Scheme 6 Schematic illustration of the CO_2 reduction process in the Z-scheme heterojunction.

In parallel, Zhang *et al.*[83] proposed a strategy to construct stable organic–inorganic Z-scheme heterojunctions by covalently linking crystalline COFs with inorganic semiconductors. A series of COF-inorganic semiconductor Z-scheme photocatalysts was synthesized by combining water-oxidation semiconductors (TiO_2, Bi_2WO_6, and α-Fe_2O_3) with CO_2-reducing COFs (COF-316/318), achieving high photocatalytic CO_2-to-CO conversion efficiencies up to 69.67 μmol g^{-1} h^{-1}. The effective covalent coupling between the organic frameworks and inorganic semiconductor components enables efficient charge transfer between the inorganic semiconductor and organic functional groups. This facilitates the accumulation of photoexcited electrons in the COF and holes in the inorganic semiconductor (*e.g.*, TiO_2), allowing them to be efficiently utilized for CO_2 reduction and water oxidation, respectively, thus mimicking natural photosynthesis. Furthermore, the coexistence of pyridine and cyano active sites within the COF photocatalysts is shown to enhance CO_2 activation and contribute significantly to the overall reduction performance.

In addition to band alignment and charge-transfer directionality, the morphology and interfacial geometry of heterostructures play a crucial role in determining their photocatalytic efficiency. Intimate contact between components with high surface area can facilitate interfacial charge transfer and maximize the exposure of active sites. Zhang *et al.*[128] developed a core–shell structured CdS@CTF-HUST-1 heterojunction photocatalyst by integrating porous covalent triazine frameworks (CTFs) with cadmium sulfide (CdS) nanospheres, achieving an impressive CO production rate of 168.77 μmol g^{-1} h^{-1} with high selectivity (Fig. 4a). Significantly, the porous CTF-HUST-1 shell endows the composite with excellent CO_2 adsorption capacity, thereby maximizing the contact probability between CO_2 molecules and active sites. Similarly, Li *et al.*[92] designed S-bridged covalent triazine framework (SCTF)/$ZnIn_2S_4$ core–shell photocatalysts that enable efficient interfacial charge transfer and spatially separated tandem reactions, namely CO_2 reduction and furfuryl alcohol (FFA) oxidation to furfural (FA) (Fig. 4b). The intimate interfacial contact and well-aligned energy levels promote electron migration from the $ZnIn_2S_4$ shell to the SCTF core. The outer $ZnIn_2S_4$ layer facilitates CO_2 diffusion toward the SCTF core, where pyridine nitrogen (Lewis base) sites act as active centers for CO_2 adsorption and activation. Simultaneously, the $ZnIn_2S_4$ shell catalyzes FFA dehydrogenation, generating additional electrons for CO_2-to-CO conversion. The optimized SCTF/$ZnIn_2S_4$-0.2 photocatalyst achieves a CO yield of

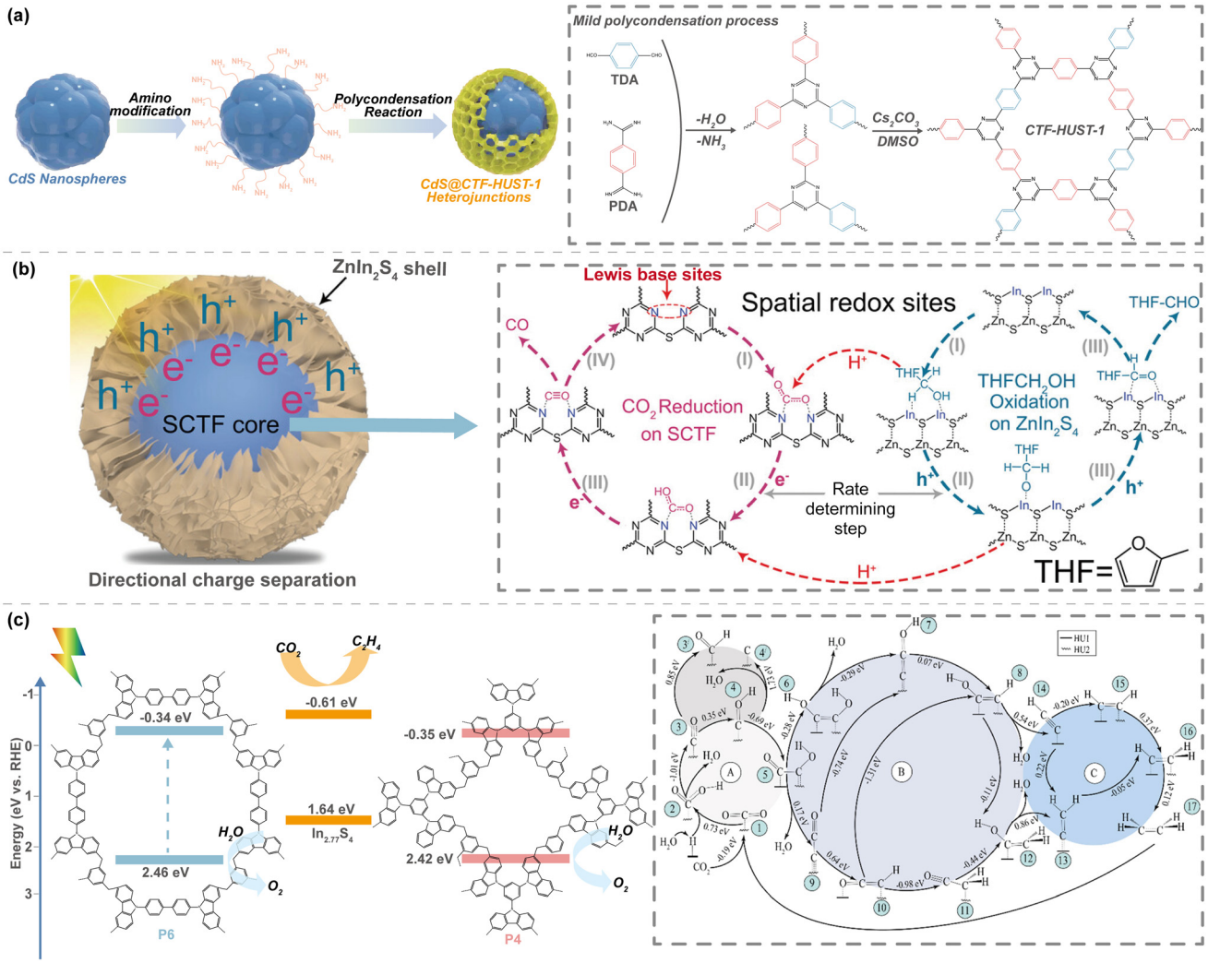

Fig. 4 (a) Schematic illustration of the synthetic routes for core–shell CdS@CTF-HUST-1 heterojunctions. Adapted with permission.[128] Copyright 2023, Wiley-VCH. (b) Illustration of the mechanism of photocatalytic CO_2 reduction and FFA oxidation on SCTF/$ZnIn_2S_4$. Adapted with permission.[92] Copyright 2024, Wiley-VCH. (c) Schematic illustration of the Z-scheme electron-transfer process of $In_{2.77}S_4$/POPs; and all possible pathways for the formation of C_2H_4 along with the corresponding free energy changes between intermediates. The CO_2-to-C_2H_4 conversion was expressed in three segments, A, B, and C, which are the formation of *OCCOH, the removal of O', and the formation of C_2H_4 from the carbide intermediate, respectively. Each intermediate was denoted by numbers (1 → 16). In segment A, the source of adsorbed hydrogen is water splitting. Adapted with permission.[93] Copyright 2023, American Chemical Society.

263.5 μmol g^{-1} and a 95% FFA-to-FA conversion under simulated solar irradiation.

In addition to C1 products, certain C2+ products arising from C–C coupling reactions have also been detected in photocatalytic CO_2 reduction. However, the formation of C2+ products typically involves complex proton-coupled electron transfer (PCET) processes and C–C bond formation, which limit their selectivity.[129] To address this challenge, Risov *et al.*[93] developed a template-free and cost-effective synthetic route to construct a composite catalyst comprising carbazole-derived porous organic polymers (POPs) integrated with $In_{2.77}S_4$. The composite is stabilized by induced-polarity-driven electrostatic interaction. Four-coordinated In^{2+} and six-coordinated In^{3+} centers function as primary active sites for facilitating CO_2 conversion to C2+ products. The synergy between the photoactive POP framework and catalytically active indium centers enhances photosensitization, gas adsorption, and catalyst dispersion. Moreover, it facilitates efficient electron transfer to C1 intermediates, promoting subsequent C–C coupling and enabling high selectivity toward C_2H_4 (98.9%), with a formation rate of 67.65 μmol g^{-1} h^{-1} (Fig. 4c).

The enhanced photocatalytic performance of the heterojunction can be attributed to several key factors: (1) internal electric fields formed at the interface facilitate directional charge transfer while retaining strong redox potentials; (2) interfacial engineering lowers the energy barrier of the rate-limiting step in the CO_2 reduction pathway; and (3) synergistic interactions between multiple components allow these systems

to overcome the intrinsic limitations of single-component photocatalysts. However, constructing an ideal semiconductor heterojunction requires close lattice matching between the constituent materials to minimize interfacial defects and suppress interfacial charge recombination.[130] This stringent requirement greatly restricts the choice of compatible materials.

3.3 Incorporating metal cocatalysts into organic polymers composed of π-conjugation units

To further enhance the performance of organic polymers composed of π-conjugation units, especially in promoting CO_2 adsorption, activation, and interfacial charge separation, the incorporation of metal cocatalysts has emerged as an effective strategy. Metal cocatalysts not only provide highly selective and accessible active sites for CO_2 adsorption and activation but also function as electron-trapping centers, facilitating efficient electron–hole separation—both of which are crucial for improving photocatalytic CO_2 reduction efficiency.[104]

The incorporation of metal cocatalysts into organic polymers can be categorized into three primary methods based on the incorporation process of the metal cocatalysts: (1) the simplest approach involves dissolving a molecular catalyst directly in the reaction medium, allowing it to be physically encapsulated within the pores of organic polymers without forming any covalent bonds between the organic polymer backbone and the cocatalyst; (2) a second strategy involves tethering the cocatalyst directly to the organic polymer backbone, typically (but not exclusively) through post-synthetic modifications. Although the cocatalyst is covalently attached to the organic polymer structure, no direct metal–ligand electronic interactions take place between the metal center and the organic polymer backbone; and (3) the third strategy incorporates metal cocatalysts by employing organic ligands directly as building blocks within the organic polymer structure itself, thus integrating the metal cocatalysts into the polymer backbone. This approach allows inner-sphere electron transfer mechanisms between the organic polymer backbone and the cocatalyst.[131] In particular, the metalation methods include both pre-synthetic and post-synthetic strategies. Pre-synthetic metalation involves the use of metal complexes directly as monomers during polymer construction. Alternatively, post-synthetic metalation serves as a flexible route for preparing metal-modified photocatalysts, allowing metal ions to be anchored onto photocatalysts through direct coordination or ligand-exchange reactions. This approach preserves the original crystallinity of the photocatalyst materials.[132] Together, these approaches provide a tunable platform for constructing metal-modified photocatalysts with high structural definition, strong interfacial charge-transfer capabilities, and excellent CO_2 activation efficiency.

Having established the functional importance of metal cocatalysts in enhancing CO_2 activation and charge dynamics within the organic polymers, various strategies have been developed to integrate metal cocatalysts through different levels of interaction strength. These approaches can be broadly categorized into three types: non-bonded incorporation, covalent tethering, and metalation (Scheme 7). Representative studies under each strategy are outlined below.

Non-bonded strategy. Recent advances have demonstrated that non-bonded strategies can also be effective in constructing high-performance systems for CO_2 photoreduction. Zhong *et al.*[87] reported the design of a synergistic photocatalyst for the selective reduction of CO_2 to CO, based on a COF incorporating single Ni sites (Ni-TpBpy). Ni-TpBpy demonstrated outstanding catalytic performance, producing 4057 μmol g^{-1} of CO over a 5 hour reaction period with a high selectivity of 96% toward CO over H_2 evolution. This outstanding activity and selectivity are attributed to the synergistic interaction between the single Ni sites and the TpBpy framework. The single Ni sites in TpBpy act as the catalytically active sites, where CO_2 molecules are coordinated, activated, and reduced. TpBpy not only serves as a host for both CO_2 molecules and single Ni sites, but also contributes to the catalytic activity and selectivity of CO_2-to-CO conversion. McQueen *et al.*[94] developed a series of hybrid photocatalysts comprising conjugated polymer semiconductors, silver nanoparticles, and a Ru-based supramolecular complex for the visible-light-driven reduction of CO_2 to formate. Among them, the hybrid photocatalyst using poly(dibenzo[*b*,*d*]thiophene sulfone) (P10) (RuRu′/Ag/P10) exhibited outstanding performance, with a TOF of 6.5 s^{-1}, a TON of 349 000, and an apparent quantum yield of 11.2% at 440 nm. The strong interaction between the sulfone units in P10 and the methyl phosphonic acid anchors of RuRu′ contributed to enhanced catalyst stability and turnover. Owing to its high durability and efficiency, RuRu′/Ag/P10 enabled quantitative CO_2 conversion, producing concentrated formate solutions up to 0.40 M.

Inspired by natural photosynthesis occurring in hierarchical networks over non-precious molecular metal catalysts, Chen *et al.*[86] reported the integration of isolated Ni sites into the hexagonal pores of polyimide-based COFs (PI-COFs). Within this architecture, the single Ni sites serve as active centers for CO_2 activation and conversion, while the PI-COFs play a dual role: functioning as photosensitizers for charge generation and providing triazine-containing structural units that promote product selectivity. A plausible intra- and intermolecular charge-transfer pathway was proposed: upon photoexcitation, electrons are generated within the PI-COF framework and efficiently migrate from the central ring to the diimide linkage, followed by transfer to the embedded Ni active sites. The observed catalytic enhancement is attributed to the synergistic interplay between the photoactive PI-COF matrix and the well-dispersed Ni centers. The nature-mimicking architecture of the PI-COFs provides a tailored microenvironment that stabilizes the Ni sites and promotes catalytic turnover.

However, the interfacial charge transfer pathway from the surface of organic polymers to the free metal complex remains insufficiently understood, warranting further in-depth investigation. He *et al.*[76] reported supramolecular photocatalytic systems consisting of COFs and Ni complexes designed for

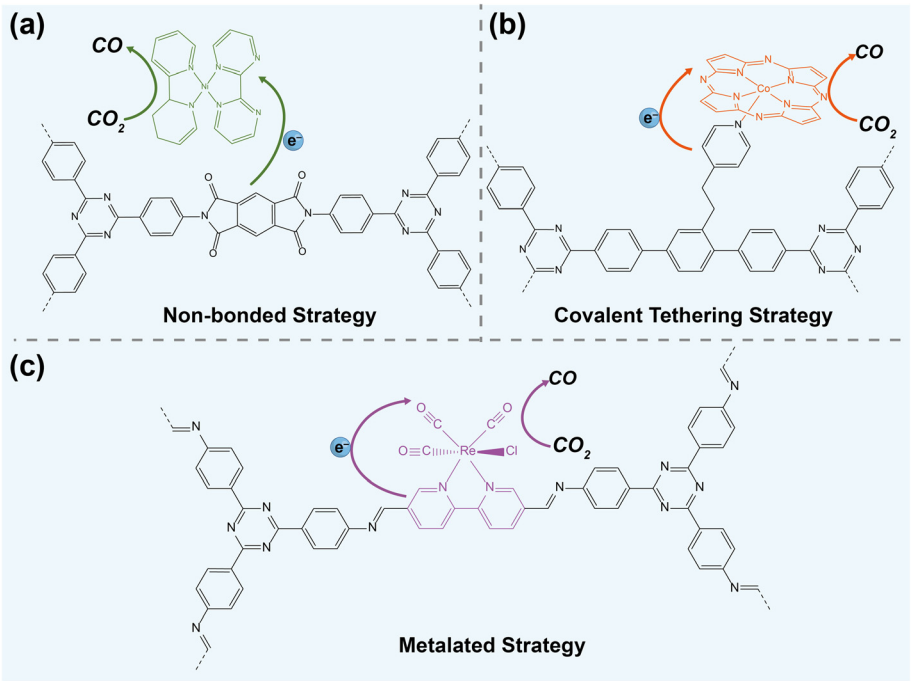

Scheme 7 Schematic illustration of the main processes for solar-to-fuel conversion with metal cocatalysts. (a) Non-bonded. Adapted with permission.[86] Copyright 2020, The Royal Society of Chemistry. (b) Covalently tethered. Adapted with permission.[133] Copyright 2024, Springer Nature. (c) Metalated organic polymers. Adapted with permission.[134] Copyright 2018, American Chemical Society. Details are provided in the text.

robust CO_2 reduction. Multiple heteroatom-mediated hydrogen bonds formed between the COF and the Ni complex were found to play a crucial role in facilitating photoinduced electron transfer across the liquid–solid interface (Fig. 5a and b). Specifically, the photocatalytic system featuring stronger hydrogen-bonding interactions exhibited outstanding CO_2 reduction capability, achieving a high CO production rate of 715 μmol g^{-1} h^{-1}, markedly outperforming systems containing only supported atomic Ni or metal complexes in the absence of such hydrogen-bond effects.

Covalent tethering strategy. Covalent binding between semiconductors and metal complexes facilitates a highly homogeneous dispersion of active sites. Wang *et al.*[133] synthesized molecular hybrid materials with precisely defined active sites by a catalyst-tethered strategy, in which a molecular catalyst is covalently anchored onto a covalent triazine framework (CTF) through coordination with pendant pyridyl ligands, resulting in a functionalized scaffold (p-CTF-py); subsequent axial coordination of a carboxyl-functionalized cobalt(II) phthalocyanine (CoTCPc) to this framework produced the hybrid photocatalyst CoTCPc@p-CTF-py. Notably, CoTCPc@p-CTF-py exhibits a charge-transfer time constant two orders of magnitude longer than that of CoTCPc@p-CTF, indicating more efficient charge separation. This rational design led to a pronounced enhancement in photocatalytic CO_2 reduction performance, achieving a CO yield of 22.1 ± 0.8 mmol g^{-1} (458 ± 17 μmol g^{-1} h^{-1}) in $KHCO_2$ aqueous buffer under visible-light irradiation. Furthermore, the covalent bonding of p-CTF-py to the molecular catalysts strongly enhances the stability of the hybrid material for CO_2 photoreduction. Similarly, Kong *et al.*[95] developed an integrated photocatalytic system (DA-CTF@DPT-Co) by covalently anchoring a cobalt 2,4-di(pyridin-2-yl)-1,3,5-triazine (DPT-Co) complex onto the extended π-conjugated framework of DA-CTF. Unlike conventional host–guest systems incorporating molecular co-catalysts, this covalent dyad enabled intramolecular cascade electron migration from the DA-CTF photosensitizer to the DPT-Co catalytic sites. This facilitated efficient charge separation and transfer, thereby enhancing overall photocatalytic activity. In addition, the broad visible-light absorption of DA-CTF, coupled with selective CO_2 adsorption and activation at the DPT-Co sites, contributed to a remarkable photocatalytic performance (Fig. 5c–f). Under visible-light irradiation for 1.5 hours, the system achieved CO and H_2 evolution amounts of 1086 and 1042 μmol g^{-1}, respectively.

Metalated strategy. *Pre-synthetic metalation* provides a powerful route for constructing active sites within conjugated frameworks. In this context, Gong *et al.*[85] developed a facile strategy to manipulate the spin state of cobalt centers within COFs by simply altering the oxidation state of cobalt in porphyrin-based COF-367-Co. COF-367-Co(III) (Co^{3+}, $S = 0$) exhibits significantly higher activity and markedly greater selectivity toward HCOOH production compared to COF-367-Co(II) (Co^{2+}, $S = 1/2$). DFT calculations indicated that COF-367-Co(III) has a lower energy barrier for the formation of HCOOH and a higher barrier for its subsequent conversion to CO and CH_4, relative to COF-367-Co(II). The theoretical results explained the observed differences in activity and product selectivity and pro-

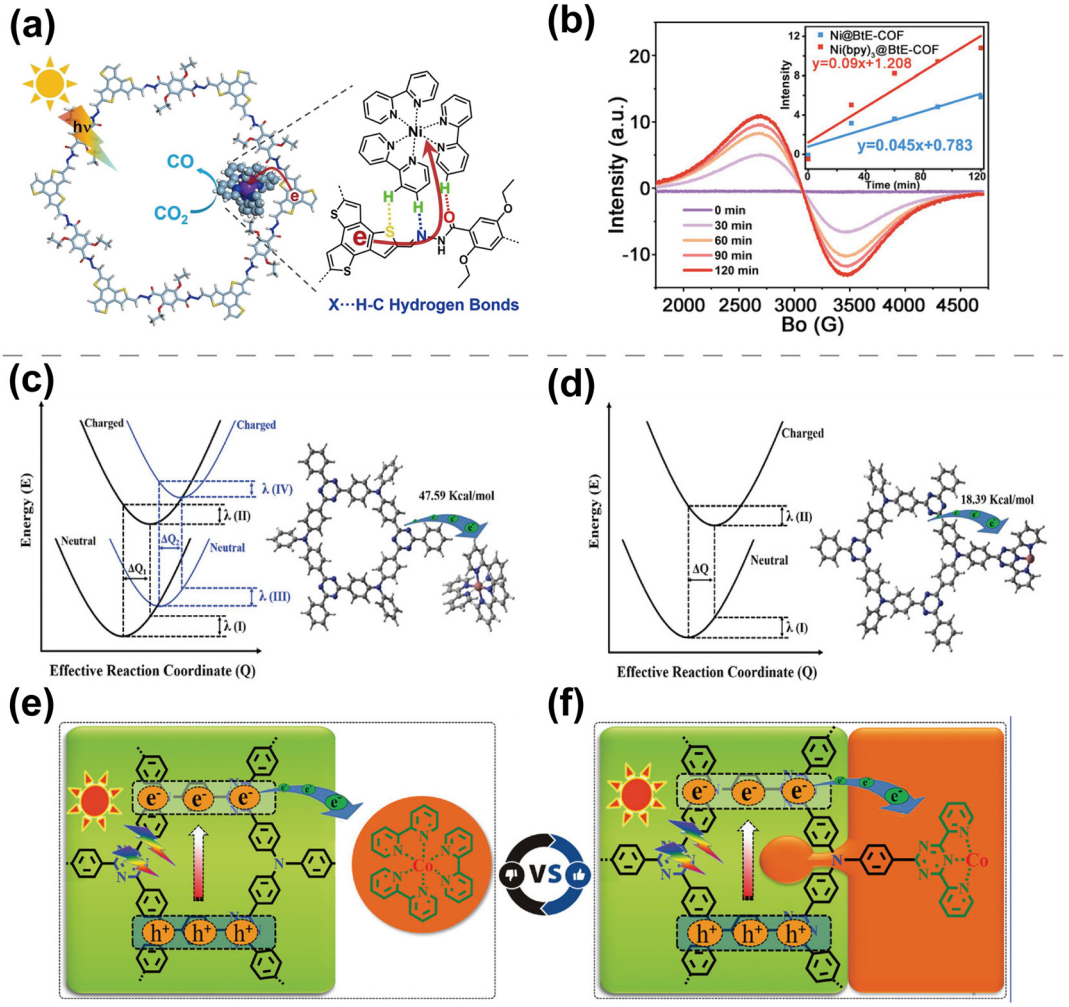

Fig. 5 (a) Schematic illustration of the electron transport *via* heteroatom-hydrogen bonds in a COF-based supramolecular photosystem for photocatalytic reduction of CO_2. Reproduced with permission.[76] Copyright 2023, Wiley-VCH. (b) EPR spectra of the Ni(bpy)$_3$@BtE-COF under light irradiation and corresponding first-order kinetics curves (inset) of the Ni(bpy)$_3$@BtE-COF and Ni@BtE-COF. Reproduced with permission.[76] Copyright 2023, Wiley-VCH. The calculated inner reorganization energy of (c) a physical mixture of DA-CTF and BPY-Co and (d) DA-CTF@DPT-Co. Reproduced with permission.[95] Copyright 2024, Wiley-VCH. A schematic illustration of the photogenerated charge migration process for (e) a physical mixture of DA-CTF and BPY-Co and (f) DA-CTF@DPT-Co. Reproduced with permission.[95] Copyright 2024, Wiley-VCH.

vided mechanistic insight into how spin-state transitions influence photocatalysis.

Besides, based on the electron-withdrawing character, the metal clusters have also been introduced into COF skeletons, denoted as metal-COFs (MCOFs), which inherited the properties and advantages of both metal–organic frameworks and COFs. For example, Li *et al.*[135] developed a fully π-conjugated, vinylene-linked multivariate D–π–A MCOF, termed UJN-1, by integrating benzyl cyanide linkers with electron-rich triphenylamine and electron-deficient copper cyclic trinuclear unit (Cu-CTU) moieties (Fig. 6a). The incorporation of Cu-CTU units, possessing strongly electron-withdrawing capabilities, introduces a significant driving force for charge separation and facilitates efficient transfer of photogenerated electrons from the triphenylamine donor to the Cu-CTU acceptor. Owing to the synergistic effect of the D–π–A configuration and the fully conjugated vinylene linkage, UJN-1 achieves highly efficient spatial charge separation. Moreover, owing to the high affinity between Cu-CTUs and CO_2 molecules, the presence of Cu-CTUs is more favorable for the adsorption and activation of CO_2 molecules during the photocatalytic reaction. As a result, it exhibits an impressive CO production rate of 114.8 μmol g^{-1} over 4 hours under visible light irradiation, without the need for any co-catalysts or sacrificial reagents.

COFs based on metal phthalocyanine possessing M-N_4 (M = Co, Cu, Ni) active sites have gained significant attention as single-atom catalysts for CO_2 reduction. Recently, Lin *et al.*[136] utilized perfluorinated metallophthalocyanine ($MPcF_{16}$) and the organic biomolecule ellagic acid (EA) as building blocks to construct functional COFs, designated as EPM-COFs (M = Co, Ni, Cu). Upon alkaline treatment (EPCo-COF-AT), the COF surface was enriched with carboxylate (COO^-) and hydroxyl

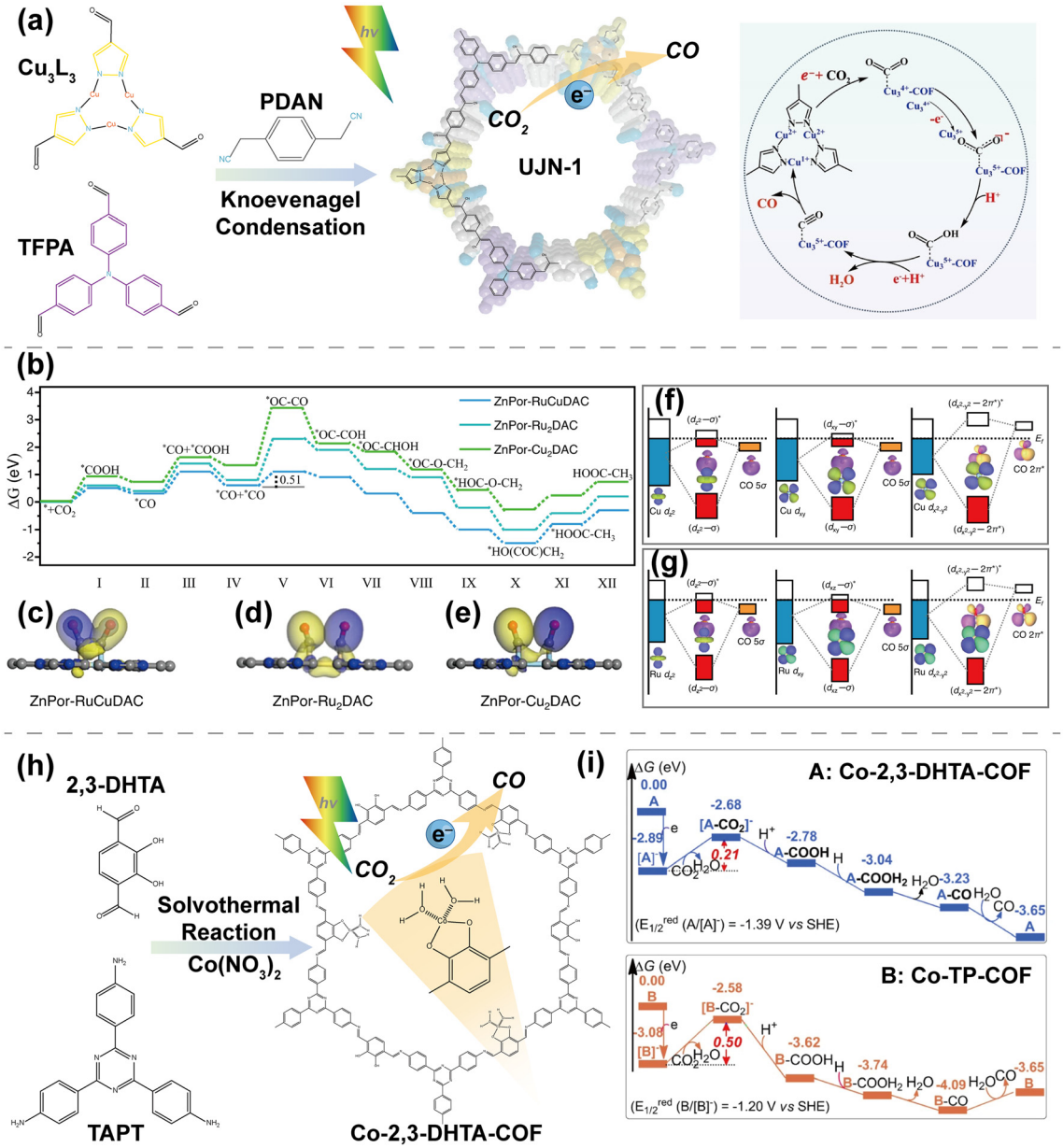

Fig. 6 (a) Schematic of the preparation and structure of vinylene-linked UJN-1. Adapted with permission.[135] Copyright 2024, Wiley-VCH. (b) Gibbs free energy diagrams of the CO_2 photoreduction to acetate pathway of ZnPor-RuCuDAC, ZnPorRu$_2$DAC, and ZnPorCu$_2$DAC. Differential charge density maps of (c) ZnPor-RuCuDAC, (d) ZnPorRu$_2$DAC, and (e) ZnPorCu$_2$DAC. Schematic illustration of the adsorbed CO (5σ, $2\pi^*$) orbital interactions with the (f) Cu 3d and (g) Ru 4d orbitals in ZnPor-RuCuDAC. Reproduced with permission.[96] Copyright 2023, Springer Nature. (h) Schematic illustration of the synthesis of a 2,3-DHTA-COF and a Co-2,3-DHTA-COF as typical examples. Adapted with permission.[137] Copyright 2023, Springer Nature. (i) Gibbs energy profiles of the CO_2RR to CO over the Co-2,3-DHTA-COF (A, blue line) and Co-TP-COF (B, orange line). Adapted with permission.[137] Copyright 2023, Springer Nature.

(OH) groups, enhancing the electron-donating capacity of EA. This modification led to a significantly improved CO production rate of 17.7 mmol g^{-1} h^{-1} and a high selectivity of 97.8%. Ultimately, the incorporation of EA into the COF enhances visible-light absorption and facilitates the PCET process essential for efficient CO_2 photoreduction. Moreover, the exposure of COO^- and OH groups in EPCo-COF-AT promotes charge transfer from EA to the Co active sites, further improving catalytic performance. Diatomic-site catalysts (DACs) have attracted considerable attention for selective CO_2 photoreduction, particularly in modulating the thermodynamic and kinetic pathways toward C2+ product formation. Wang *et al.*[96] synthesized AB-stacked heteronuclear dual-atom-site COFs through the self-assembly of Zn-porphyrin and Ru/Cu-pincer complexes. Under light irradiation, efficient intraskeletal electron transfer occurred from the Zn center to the adjacent diatomic catalytic sites. Electronic structure analyses of key CO intermediates revealed that the heteronuclear Ru–Cu

active site exhibited pronounced Ru 4d–Cu 3d gradient orbital coupling, resulting in asymmetric charge distribution across the two adjacent CO intermediates. These intermediates were stabilized in a side-by-side configuration on the Ru and Cu atoms, thereby lowering the energy barrier for C–C coupling (Fig. 6b–g). Consequently, the heteroatomic ZnPor-RuCuDAC achieved the highest acetate selectivity of 95.1%, significantly surpassing those of ZnPor-Cu_2DAC (36.9%) and ZnPor-Ru_2DAC (21.6%). Notably, ZnPor-Cu_2DAC exhibited the highest selectivity toward CO production.

Post-synthetic metalation enables versatility by introducing metal centers into preformed organic polymers, offering a tunable platform for enhancing photocatalytic activity. Zhang *et al.*[137] designed two types of Co-based COF (Co-COF) catalysts featuring oxygen-coordinated cobalt centers, and demonstrated that fine-tuning the coordination environment significantly enhances photocatalytic performance (Fig. 6h). In particular, the Co-COF with Co–O_4 coordination sites achieved an outstanding CO production rate of 18 000 μmol g^{-1} h^{-1} and a high selectivity of 95.7% under visible-light irradiation. The optimized coordination environment not only improved the loading capacity of Co(II) within the COF but also facilitated more efficient electron transfer from the photosensitizer to the catalytic sites and enhanced CO_2 adsorption. Furthermore, the Co-2,3-DHTA-COF enriched with Co–O_4 active sites significantly reduced the energy barrier of the rate-determining step (ligand exchange between Co-2,3-DHTA-COF and CO_2).

In addition, Cheng *et al.*[78] developed a porous material with a crystalline topological framework, named viCOF-bpy-Re, which was rationally synthesized *via* a post-synthetic strategy by incorporating rhenium complexes as reductive sites and triazine ring structures as oxidative sites, connected through robust –C═C– linkages. The charge-separation efficiency of viCOF-bpy-Re is enhanced by the presence of low-polarity π-bridges between the rhenium complexes and triazine units, facilitating efficient intramolecular charge transfer. As a result, viCOF-bpy-Re exhibits outstanding photocatalytic performance, achieving a CO production rate of 190.6 μmol g^{-1} h^{-1} with nearly 100% selectivity, along with O_2 evolution at 90.2 μmol g^{-1} h^{-1}. Recently, Ishihara *et al.*[97] designed ternary conjugated polymers incorporating a Ru-complex catalytic unit, denoted as $[Cz\text{-}DbtO\text{-}Ru]_n$. By leveraging the structural tunability of conjugated polymers, they systematically modulated the cascade energy levels through molecular-level control over the composition and sequence of building blocks. Spectroscopic characterization and theoretical modeling revealed that the cascade energy alignment in $[Cz\text{-}DbtO\text{-}Ru]_n$ facilitated efficient long-range charge separation *via* directionally selective electron transfer from the photoexcited π-system to the Ru catalytic center. Among the evaluated compositions, the optimized ternary polymer $[Cz_2\text{-}DbtO_3\text{-}Ru_1]_n$ showed the highest performance, achieving external quantum efficiencies of 9.0% (with TEOA) and 32.2% (with benzimidazole derivative (BIH)) at 450 nm, along with a formate yield up to 0.48 M.

In another example, Zhu *et al.*[71] reported a cobalt-metalated, one-dimensional (1D) ABC-stacked COF (PP-COF-Co), which integrates perylene diimide (PDI) as a photosensitizer and 1,10-phenanthroline as a metal coordination site. PP-COF-Co exhibits a 57-fold increase (37.9 mmol g^{-1}) in photocatalytic CO_2 reduction activity compared to its pristine analogue (0.67 mmol g^{-1}). Mechanistic investigations indicate that the dispersed PP-COF-Co photocatalyst provides abundant exposed Co active sites, promoting efficient CO_2 capture. Upon photoexcitation, electrons migrate from the organic framework to the Co centers through the Co–C charge-transfer bridge, enabling long-lived charge separation and effective CO_2 reduction to CO.

To elucidate the atomic-level correlation between active sites and photoreduction activity, Ran *et al.*[80] developed a universal synthetic protocol for fabricating single-atom metal sites (SASs) anchored on triazine-based COFs (Tr-COFs), resulting in a series of catalysts denoted as SAS/Tr-COF. This strategy enables the incorporation of various metal centers (*e.g.*, Fe, Co, Ni, Zn, Cu, Mn, and Ru) *via* a metal–nitrogen–chlorine bridging structure for high-performance CO_2 photoreduction. Among them, the Fe SAS/Tr-COF, serving as a representative photocatalyst, exhibited an impressive CO production rate of 980.3 μmol g^{-1} h^{-1} and a selectivity of 96.4%—more than 26 times higher than that of the pristine Tr-COF under visible-light irradiation. DFT calculations revealed that the enhanced photocatalytic performance arises from the synergistic interaction between the atomically dispersed Fe sites and the Tr-COF framework. This synergy effectively lowers the energy barrier for the formation of *COOH intermediates, while also promoting CO_2 adsorption and activation, and CO desorption. Similarly, Fu *et al.*[98] developed a bipyridine-functionalized COF (TPy-COF) for the immobilization of isolated Co sites (TPy-COF–Co), enabling photocatalytic CO_2 reduction to syngas. In this system, triazine units within the framework facilitate charge separation and transfer, while bipyridine moieties provide precisely defined coordination sites for Co atoms. The resulting TPy-COF-Co exhibited a record-high CO production rate of 426 mmol g^{-1} h^{-1}, along with turnover number (TON) and turnover frequency (TOF) values of 2095 and 1607 h^{-1}, respectively. Moreover, the catalyst demonstrated excellent recyclability and tunable syngas composition, with CO/H_2 ratios ranging from 1.8 : 1 to 1 : 16. Mechanistic studies revealed a directional charge transfer pathway: electrons are transferred from $[Ru(bpy)_3]Cl_2$ to the COF backbone and subsequently to the Co centers after hole quenching. The triazine-based framework promotes charge delocalization, facilitating the generation of low-valent Co species necessary for CO_2 activation. Moreover, the Co–N_4Cl_2 coordination environment stabilizes *COOH intermediates and reduces the activation barrier, collectively contributing to the enhanced photocatalytic performance.

To achieve synergistic action of these active metal sites, their uniform distribution and easy accessibility are prerequisites for high photocatalytic activity and selectivity. In this context, Geng *et al.*[72] designed a tandem photocatalytic strategy based on sequential post-synthetic metalation (SPSM) of variable Ru/Co sites into a trinuclear copper-based COF, Cu_3-BPY-COF, to construct a series of tri-metallized frameworks,

denoted Cu_3-BPY-COF(Ru/Co)-*X* (*X* = 1, 2, or 3, corresponding to Ru : Co molar ratios of 1/39.6, 1/19.6, and 1/12.7, respectively), for selective photocatalytic CO_2 methanation. The incorporation of a small fraction of Ru sites enhances visible-light absorption, while Co sites, immobilized at the bipyridine units, facilitate efficient CO generation and local enrichment around the active trinuclear Cu centers. This cooperative interaction significantly boosts the catalytic efficiency for CO_2 reduction to CH_4. Notably, the optimized Cu_3-BPY-COF(Ru/Co)-2 achieved an outstanding CH_4 evolution rate of 31.5 μmol g^{-1} h^{-1} and a high selectivity of 95%, representing a 15-fold enhancement over the Ru-only variant, Cu_3-BPY-COF(Ru).

While photocatalytic CO_2 reduction has predominantly yielded C1 products, the formation of C2+ products remains challenging, largely due to the limited ability of single-metal active sites to promote C–C coupling. Drawing inspiration from tandem catalysis in multi-enzyme systems, Zhang *et al.*[99] designed a porous organic polymer (POP) incorporating atomically dispersed Cu and Mo dual-metal centers (CuPor-POP-Mo), enabling cascade catalysis for selective C_2H_6 production (Fig. 7a). The system exhibited a C_2H_6 evolution rate of 472.5 μmol g^{-1} h^{-1}, with 87.5% product selectivity. Mechanistic studies suggest that photoexcited $[Ru(bpy)_3]Cl_2$ transfers electrons through the delocalized π-framework of the POP to the Cu and Mo sites (Fig. 7b). Initial reduction of CO_2 to *CO occurs at the Cu centers, followed by spillover of *CO to adjacent Mo sites, where *CO accumulation facilitates *OCCO intermediate formation. Subsequent hydrogenation and deoxygenation steps, mediated cooperatively by Cu and Mo, lead to the formation of C_2H_6 (Fig. 7c). Concurrently, triethanolamine (TEOA) acts as a sacrificial electron donor, completing the photocatalytic cycle.

Collectively, these studies highlight the versatility of metal cocatalyst integration in the organic polymer-based CO_2 photoreduction systems by facilitating charge carrier modulation, tuning reaction pathways, and enhancing product selectivity. Central to this progress is the synergistic interplay between precisely defined metal active sites and the π-conjugated polymer matrix. Nevertheless, the mechanistic understanding of such synergistic effects remains incomplete. While dual-site single-atom metal cocatalysts have been extensively explored in electrocatalysis, their application in photocatalysis remains

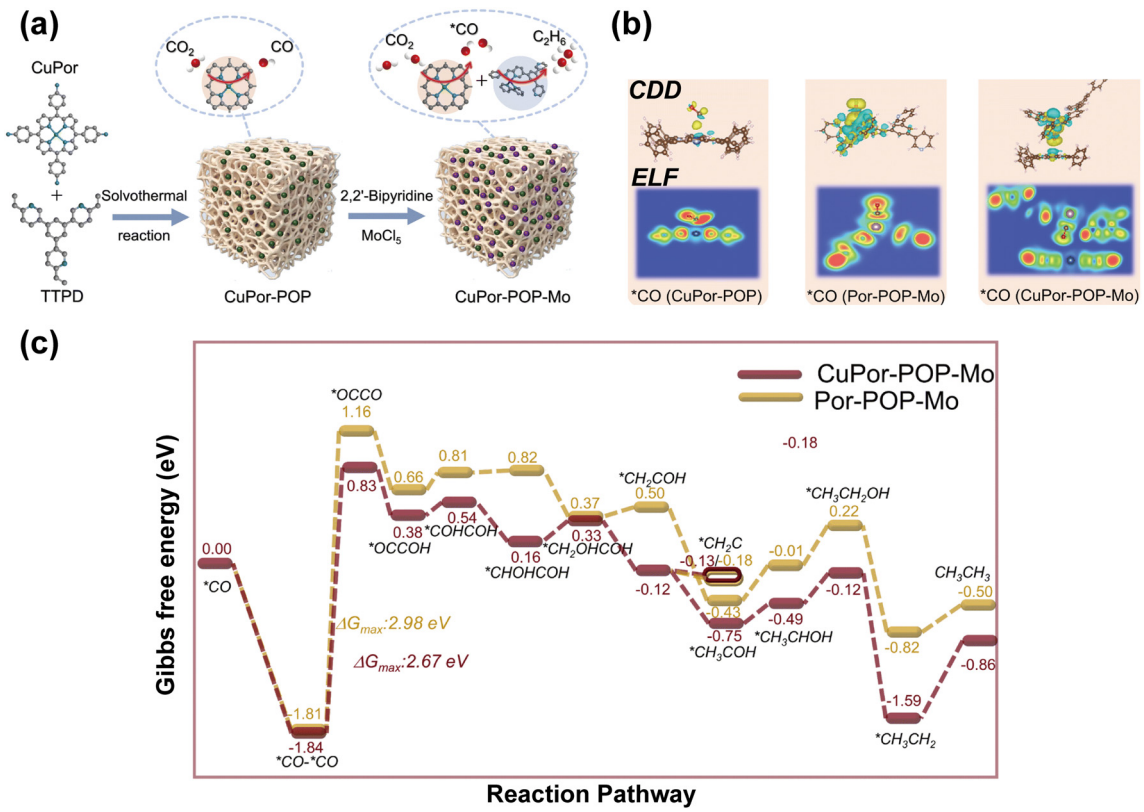

Fig. 7 (a) Schematic illustration of the synthesis of CuPor-POP-Mo and photocatalytic CO_2 reduction. The amine monomer is 5,10,15,20-tetrakis(4-aminophenyl)-21*H*,23*H*-porphine-Cu(ii) (CuPor), and the aldehyde monomer is 5,5′,5″-(benzene-1,3,5-triyl)tripicolinaldehyde (TTPD). Reproduced with permission.[99] Copyright 2025, The Royal Society of Chemistry. The density functional theory (DFT) calculations and Gibbs free energy change of the reaction. (b) Charge density difference (yellow and cyan areas with an isosurface value of 0.0005 indicate charge accumulation and depletion, respectively). Carbon atoms are presented in light brown, O atoms in red, Cu atoms in dark blue, N atoms in light blue, and Mo atoms in purple. Reproduced with permission.[99] Copyright 2025, The Royal Society of Chemistry. (c) Gibbs free energy profiles of the CO_2RR to C_2H_6 over CuPor-POP-Mo and Por-POP-Mo. The "*" represents adsorption on the substrate. Reproduced with permission.[99] Copyright 2025, The Royal Society of Chemistry.

largely untapped. Designing complementary dual-metal catalytic sites represents a promising strategy to achieve high selectivity in CO_2 photoreduction.

3.4 Morphological tuning

In addition to molecular-level design, morphological regulation of the organic polymers has emerged as a crucial strategy for enhancing photocatalytic CO_2 reduction. Specifically, low-dimensional nanomaterials possess abundant unsaturated atomic sites on their surfaces and edges, which serve as active sites for the adsorption/desorption of CO_2 and key intermediates in catalytic reactions. For example, polymer dots (Pdots) are a subclass of polymer nanoparticles with diameters below 100 nm. Their small size results in a high surface area, which improves interfacial charge separation and helps overcome the short exciton diffusion lengths typical of organic polymers.[138] Pdots can be formed by using amphiphilic polymers as surfactants, which stabilize the polymers in water, increase surface area, and concentrate charges within individual particles. These features are beneficial for catalytic reactions in water requiring multiple charges.[79] To further investigate the advantage of Pdots in photocatalytic CO_2 reduction, Cai *et al.*[79] reported that Pdots composed of poly[(9,9′-dioctylfluorenyl-2,7-diyl)-*co*-(1,4-benzothiadiazole)] (PFBT) can photocatalytically reduce CO_2 to CO in aqueous solution without adding any extra co-catalyst (Fig. 8a). These PFBT Pdots achieved a CO production rate of 57 μmol g^{-1} h^{-1} with a selectivity of up to 100%. Mechanistic investigations revealed that the photoexcited PFBT Pdots are initially reduced by the sacrificial donor, after which the reduced Pdots bind CO_2 and facilitate its conversion to CO through intrinsic active sites. DFT calculations further confirmed that the microenvironment within the Pdots plays a key role in promoting the CO_2 reduction reaction, enabling the transfer of multiple electrons *via* the benzothiadiazole units (Fig. 8b).

Ultrathin 2D organic polymers, with a nanoscale thickness or even when reduced to the sub-nanometer level, further shorten the migration distance of photogenerated carriers and enhance the light absorption cross-section.[139] The dimensional reduction of photocatalysts from bulk structures to nanosheet morphologies can enhance photocatalytic performance by increasing specific surface area for improved CO_2 adsorption and facilitating more efficient charge transport.[140] Typically composed of fewer than ten stacked monolayers, these nanosheets exhibit nanoscale thickness and a quantum size effect.[141] For example, 2D COF nanosheets (NSs) have shown promising potential in heterogeneous photocatalysis due to their large surface area, abundant active sites, and enhanced substrate contact facilitated by a lower diffusion barrier. Liu *et al.*[90] reported a scalable, bottom-up synthetic strategy for the facile preparation of ultrathin (<2.1 nm) imine-based 2D COF NSs—including COF-366 NSs, COF-367 NSs, COF-367-Co NSs, TAPB-PDA COF NSs, and TAPB-BPDA COF NSs (Fig. 8c). This novel synthetic approach effectively limits axial π–π stacking, enabling the successful fabrication of ultrathin, imine-linked 2D COF NSs. In this photocatalytic system, the large aspect ratio and 2D morphology of COF-367-Co NSs provide a high density of accessible active sites on their surface. This configuration results in outstanding photocatalytic efficiency, with a CO production rate as high as 10 162 μmol g^{-1} h^{-1} and a selectivity of approximately 78% under visible-light irradiation in aqueous media.

Also, for organic polymers, precisely defined pore structures can enhance their mass transfer processes and maximize the accessibility of catalytic sites.[142,143] Besides, porous photocatalytic systems with intrinsic nanoconfinement offer a unique opportunity to improve selectivity, as the spatial confinement of reaction intermediates favors C–C coupling.[144,145] Rational control over pore size distribution is essential for optimizing photocatalytic performance. Micropores (<2 nm) enhance the accessibility of active sites by enabling efficient diffusion and confinement of CO_2 molecules within the pore channels. The incorporation of mesopores (2–50 nm) enhances the diffusion of reactants and products, alleviating mass transfer limitations. However, excessively large pore sizes may lead to low conductivity by preventing communication between adjacent units,[146] and decrease the density of accessible active sites, ultimately compromising CO_2 conversion efficiency.[147] Therefore, it is possible to design catalysts with specific morphologies to fully leverage the advantages of low-dimensional nanostructures and porous structures, thereby achieving higher efficiency and selectivity in the field of CO_2 photoreduction. Wang *et al.*[100] developed conjugated porous aromatic frameworks (PAF-332-DCM and PAF-332-DCE) *via* a cost-effective Friedel–Crafts reaction. By incorporating conjugated coronene units, the resulting π-conjugated frameworks exhibit broad near-infrared (NIR) light absorption and tunable porosity. The enhanced porosity affords abundant surface sites for CO_2 adsorption and diffusion, effectively addressing the mass transport and accessibility issues associated with non-porous structures. Among the synthesized materials, PAF-332-DCM demonstrated superior photocatalytic CO_2 reduction performance, achieving a CO evolution rate of 74.7 μmol g^{-1} h^{-1} and maintaining high structural stability over 30 hours of continuous operation. The improved activity was ascribed to the synergistic integration of the continuous π-conjugated structure, high CO_2 uptake capacity, and efficient NIR-driven catalytic response. Zhao *et al.*[101] synthesized two pyrene-based one-dimensional covalent organic frameworks (COFs), PyPDA-COF and PyPDB-COF, with distinct pore sizes. Although Co-PyPDA-COF and Co-PyPDB-COF shared similar 1D chain architectures, Co(II) coordination environments, and metal loadings, Co-PyPDA-COF featured significantly smaller pores. As a result, the Co-PyPDA-COF exhibited a markedly enhanced CO evolution rate of 30.5 mmol g^{-1} h^{-1} and a CO selectivity of 95.8% over 2 hours, outperforming Co-PyPDB-COF (17.7 mmol g^{-1} h^{-1} and 93.6%). The superior performance of the Co-PyPDA-COF was attributed to its reduced pore size, which imparted multiple benefits (Fig. 8d and e): shortened distances between adjacent Co(II) sites enabling dual-site interaction with a single CO_2 molecule, and shortened photoelectron transfer distance, facilitating more efficient charge transport.

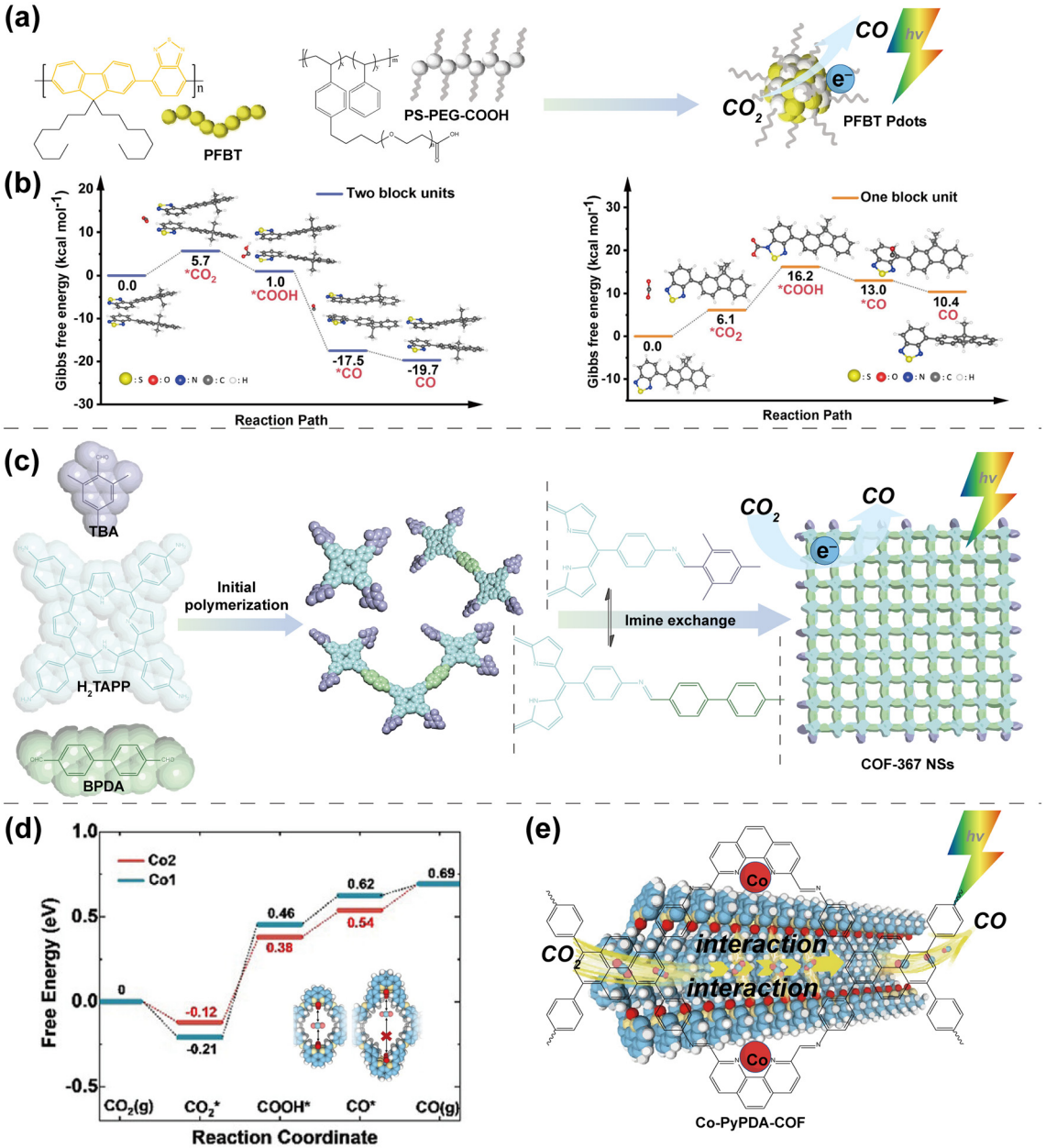

Fig. 8 (a) Illustration of the structures of PFBT, PS-PEG-COOH, and the corresponding Pdots. Adapted with permission.[79] Copyright 2023, Wiley-VCH. (b) The energy panel of the reaction pathway on (left) the two adjacent reduced block units; (right) the one block unit. Reproduced with permission.[79] Copyright 2023, Wiley-VCH. (c) Schematic illustration of the synthesis of the COF-367 NSs. Adapted with permission.[90] Copyright 2019, American Chemical Society. (d) Plot of Gibbs free energy for the reduction of CO_2 to CO. Inset: the coordination mode of CO_2 with Co(II) sites within the pores of the Co-PyPDA-COF (left) and Co-PyPDB-COF (right). Adapted with permission.[101] Copyright 2025, Wiley-VCH. (e) Schematic diagram of CO_2 photoreduction in the Co-PyPDA-COF host. Adapted with permission.[101] Copyright 2025, Wiley-VCH.

4 The construction of highly active and stable organic supramolecules composed of π-conjugation units for CO_2 photoreduction

Organic supramolecules composed of π-conjugation units are formed *via* bottom-up self-assembly of π-conjugated monomers, governed by extended π-conjugation and intermolecular interactions. When π-conjugated monomers are assembled, the overlap of π-orbitals creates extended conjugation pathways that alter their electronic structure. Crucially, the degree of π-orbital overlap determines the extent of electronic delocalization.[148] Therefore, organic supramolecules composed of π-conjugation units exhibit remarkable tunability in both the chemical structure and optoelectronic properties, similar to the organic polymers. Many of the strategies previously discussed for organic polymers are also applicable to supramole-

cular systems. For D–A engineering, Liao and colleagues[149] developed an A–D–A type supramolecular photocatalyst based on *N*,*N*′-bis(4-fluorophenyl)perylene-3,4,9,10-bis(dicarboximide) (PDIBF), which enabled the selective photoreduction of CO_2 and water vapor to C_2H_6. The A–D–A architecture resulted in a redistribution of the surface electrostatic potential, with electrons accumulating on the fluorobenzene and carbonyl groups, and holes being localized on the perylene core. This separation induced a strong internal electric field that enhanced charge separation and suppressed recombination. For the strategy of building semiconductor heterojunctions, Xu *et al.*[150] constructed a two-dimensional organic–inorganic heterojunction (NiAl-ZnTCPP) by electrostatically assembling anionic Zn-porphyrins onto layered double hydroxide (LDH) surfaces. The interfacial electric field promoted directional charge flow to the porphyrin moieties, improving both selectivity (98%) and activity (1568.6 μmol g^{-1} h^{-1}). Gai *et al.*[151] further reported a photosynthetic biohybrid system by coating *Moorella thermoacetica* with a p–n heterojunction (PFP/PDI) *via* electrostatic and hydrophobic interactions. This configuration enabled direct electron transfer from the heterojunction to the bacteria, bypassing redox shuttles and activating the Wood–Ljungdahl pathway for light-driven acetic acid production from CO_2. Given that these approaches parallel those employed in CP-based systems, they are not reiterated in the following section.

The primary distinction between organic supramolecules composed of π-conjugation units and the previously discussed organic polymers lies in their mode of structural connectivity. Organic supramolecules, including HOFs, SOFs, and related supramolecular assemblies, each incorporating π-conjugated units, self-assembled with organic π building blocks through hydrogen-bonding, π–π stacking, and other non-covalent interactions (Scheme 8). These interactions enable organic π building blocks to spontaneously and hierarchically organize into functional supramolecular architectures with semiconductor properties.[152] A notable feature of these noncovalent systems is the cooperative nature of intermolecular interactions, wherein the collective effect of multiple weak forces exceeds the sum of individual contributions.[153] Therefore, the dynamic behavior and flexibility of noncovalent interactions can endow organic supramolecules with unique properties in the field of CO_2 photoreduction, as follows:

(1) Compared to covalent bonds within organic polymers, taking advantage of the high reversibility of noncovalent interactions, the developed supramolecular systems have the potential to be easily processed and recycled, which can substantially lower the cost in photocatalysis. More importantly, organic supramolecules composed of π-conjugation units can be endowed with the ability to repair themselves after damage, which is commonly called "self-healing" and is of great significance in extending the durability of materials.[154] For example, the weak hydrogen bonds, in cooperation with interlayered π–π interactions, enable the functionalization of HOFs through simple solution-assisted sonication exfoliation and post-synthetic modification. Jiang and colleagues[155] reported that the post-modification of a guanine-quadruplex-linked 2,2′-pyridine-containing HOF (HOF-25) with $Ni(ClO_4)_2{\cdot}6H_2O$, followed by sonication exfoliation, afforded HOF-25-Ni nanosheets (NSs) with high yield. Notably, the collected dry HOF-25-Ni NSs retain high crystallinity due to the reassembly of the thin NSs. Atomic Ni sites were successfully immobilized on 20% of the 2,2′-pyridine moieties in the crystalline HOF-25-Ni. The increased CO production was attributed to the enhanced density of active Ni sites. Furthermore, HOF-25 could also be post-modified with $Re(CO)_5Cl$ to afford HOF-25-Re.[156] The regenerated HOF-25-Re, obtained through recrystallization followed by post-functionalization, exhibited restored photocatalytic performance.

(2) The non-covalent interactions can be precisely and reasonably modulated with various parameters, including pH, temperature, concentrations, and solvents, thereby enabling supramolecular materials with diverse morphologies and tunable architectures.[157] For example, strong π–π interactions between perylene rings facilitate the self-assembly of perylene diimide (PDI) molecules into ordered organic semiconductors with defined crystal structures and controllable morphologies *via* the simple phase-transition method.[158] Ma *et al.*[159] reported a stepwise approach for fabricating uniform nanotubes by integrating bottom-up and top-down processes. The introduction of sterically hindered groups at the 2-position of benzyl substituents on asymmetric PDI molecules directed the formation of a kinetically trapped microribbon ("bottom-up"), which subsequently broke into nanowires ("top-down") and ultimately transformed into thermodynamically stable nanotubes. In another example, Liu *et al.*[160] synthesized tetragonal ZnTPyP nanorods (T-ZnTPyPs) and hexagonal nanowires (H-ZnTPyPs) by varying the assembly temperature. Elevated temperatures affected the structural integrity and functional properties of the emulsifier templates, thereby influencing intermolecular interactions within the assembly microenvironment. As a result, incubation temperature governed both the morphology of the emulsifier template and the nucleation and growth kinetics, leading to distinct ZnTPyP stacking arrangements.

(3) The π-conjugated self-assembled units provide a significant contribution to the fundamental optoelectrical properties of supramolecular materials, while the non-covalent interactions offer the possibility to tune photophysical processes such as charge transport and exciton recombination.[161]

Every coin has its two sides: while the dynamic and reversible nature of noncovalent bonds enables recyclability and

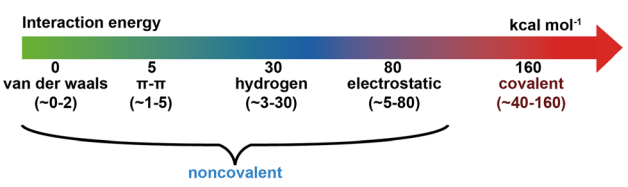

Scheme 8 The approximate range of different interaction energies. Adapted with permission.[162] Copyright 2025, Wiley-VCH.

reorganization, it simultaneously renders supramolecular systems susceptible to heat, water, and/or solvents, leading to poor stability. Elevated temperature increased molecular kinetic energy and weakened these interactions; penetration of water or organic solvents into the assemblies disrupted the noncovalent contacts and disintegrated the networks.[153] Moreover, supramolecular assemblies based on noncovalent interactions still faced challenges, including complexity arising from tautomerism of the molecular building units, the assembly process itself, and the structural versatility of the building blocks.[163]

Given the essential role of structural stability in photocatalytic performance, further exploration of design approaches is necessary. A fundamental understanding of structure–function relationships remained essential for the rational design of stable and efficient π-conjugated supramolecular systems. The π-conjugated self-assembled units are one of the basic factors that influence the structural stability and photocatalytic performance of supramolecular materials. The geometric features of the π-units—such as their shape, length, and spatial conformation—as well as their functional groups and the availability of multiple noncovalent interaction sites directly influence the molecular packing order (*i.e.*, crystallinity), degree of π-conjugation (*via* π–π stacking), band structure, morphology, and charge transport behavior.[164–166] At the same time, the extent of π–π stacking and the presence of multiple noncovalent interactions are decisive in governing the structural stability of the supramolecular systems.[167,168] Nevertheless, a comprehensive understanding of how these structural parameters affect the stability and function of organic supramolecules composed of π-conjugation units remains limited and requires further systematic investigation. Moreover, directing π-units to assemble into specific motifs remains challenging, as they are often trapped in kinetically stable yet topologically diverse arrangements.[169] Effective assembly strategies that enable control over aggregation states are therefore needed to construct structurally defined supramolecular architectures.

4.1 Diversity of π-conjugated self-assembled units

Studies on organic supramolecules composed of π-conjugation units for CO_2 reduction remain relatively scarce, as summarized in Table 2. Here, we highlight several representative examples, with a particular focus on recently reported porphyrin/pyrene-based supramolecular assemblies and novel supramolecular photocatalysts.

Porphyrin units. As key active centers in natural enzymatic systems, porphyrins have been extensively employed in the design of artificial enzymes and serve as promising building blocks for photocatalytic applications.[176] In recent years, π-conjugated porphyrins have attracted particular interest owing to their outstanding photophysical, photochemical, electrochemical, and structural properties. Their broad and intense light absorption enables efficient utilization of the solar spectrum. Furthermore, the rigid and planar molecular skeleton, along with the aromatic electronic structure, facili-

Table 2 Organic supramolecules composed of π-conjugation units for photocatalytic CO_2 reduction

Photocatalyst	Catalyst dosage	Reaction medium	Light source	Rate max. ($\mu mol\ g^{-1}\ h^{-1}$)	Selectivity [%]	Stability [h]	AQY [%]	Isotope-labeling experiments	Oxidation products [$\mu mol\ g^{-1}\ h^{-1}$]	Ref.
HCDS	5 mg	H_2O/TEOA (9 : 1, 5/v)	300 W Xe lamp	C_2H_6, 250.9	64.2	40	21.5	YES	—	170
Nalg-4	0.2 mM	TEA·HCl, 5% TEA	300 W Xe lamp	CH_4, 13 000	89	>720	15.1	YES	—	171
FC1	0.35 mg	MeCN/BIH/TFE	300 W Xe lamp ($400 \leq \lambda \leq 750$ nm)	CO, 29 100	99.9	96	0.298	YES	—	172
PFC-58–30	5 mg	H_2O	300 W Xe lamp ($\lambda > 400$ nm)	CO, 7.27; HCOOH, 29.8	—	10	—	YES	H_2O_2	173
PFC-58	5 mg	H_2O	300 W Xe lamp ($\lambda > 400$ nm)	CO, 3.16; HCOOH, 5.9	—	10	—	YES	H_2O_2	173
PFC-58–61	5 mg	H_2O	300 W Xe lamp ($\lambda > 400$ nm)	CO, 4.25; HCOOH, 15.7;	—	10	—	YES	H_2O_2	173
PFC-72-Co	3.5 mg	Gas–solid regime; H_2O/TEOA (9 : 1, v/v)	300 W Xe lamp ($\lambda > 400$ nm)	CO, 14.7	—	2	—	YES	—	174
PFC-73-Ni	3.5 mg	Gas–solid regime; H_2O/TEOA (9 : 1, v/v)	300 W Xe lamp ($\lambda > 400$ nm)	CO, 9.8	—	2	—	YES	—	174
PFC-73-Cu	3.5 mg	Gas–solid regime; H_2O/TEOA (9 : 1, v/v)	300 W Xe lamp ($\lambda > 400$ nm)	CO, 4.4	—	2	—	YES	—	174
Ullazine supramolecular polymers	—	CH_3CN/H_2O (4 : 1, v/v)	Blue LEDs (450 nm)	$TON_{CO} = 4645 \pm 306$, $TON_{CH_4} = 1518 \pm 205$	—	144	—	—	—	175
PDIBF	100 mg	H_2O	300 W Xe lamp ($\lambda > 420$ nm)	C_2H_6, 83	85	50	1.6	YES	O_2	149

tates the assembly of porphyrins into precisely defined nanostructures with favorable optoelectronic properties. Notably, since porphyrin self-assembly primarily relies on diverse intermolecular noncovalent interactions, nanostructures with specific sizes, shapes, and functions can be achieved through careful molecular and supramolecular design. As a result, porphyrin-based nanostructures have been widely applied in visible-light photocatalysis.[177]

A unique advantage of porphyrins lies in their capacity to coordinate a wide range of metal ions into the central cavity, forming metalloporphyrins that often serve as catalytic centers for CO_2 photoreduction. The metalloporphyrin core plays a pivotal role in tuning the electronic structure and governing the catalytic activity.[178] *Metalloporphyrins* possess a stable tetrapyrrolic conjugated macrocyclic structure with an $M–N_4$ coordination environment, where M represents the central metal.[179] In organic supramolecules composed of π-conjugation units, metalloporphyrins act as structural units, with the $M–N_4$ sites serving as catalytic centers.[180] Notably, the nature of the metal affects the extent of through-ligand orbital overlap (conjugation) and the strength of weak peripheral interactions.[174] Given that even subtle differences in coordination environments can significantly impact photocatalytic performance, elucidating clear structure–activity relationships remains a significant challenge in the rational design of metalloporphyrin-based supramolecular photocatalysts.

In particular, porphyrinic building blocks with different metal centers may influence the self-assembly results and the stability of HOFs. With this consideration, Liu and colleagues[174] reported that, under topological guidance, the self-assembly process based on a tetratopic porphyrin synthon resulted in a HOF with the predicted square layer (sql) topology, but with unsatisfactory stability (Fig. 9a). Metallizing the porphyrin centers generated an identical network, yet with greater orbital overlap between the interlamellar porphyrin cores, thereby significantly improving structural stability. Strikingly, metallization of the porphyrin core drastically altered the π–π stacking, and thus the noncovalent interactions between adjacent porphyrin rings in different layers. Theoretical studies further elucidated this transformation from the perspectives of the electronic structure and orbital overlap. In addition to enhanced robustness, metallization of the porphyrin center imparted the frameworks with distinct catalytic activities toward CO_2 photoreduction, among which PFC-72-Co (14.7 μmol g^{-1} h^{-1}) shows the optimal performance.

Pyrene unit. Pyrene-based molecules exhibit excellent electronic and optical physical properties and especially excellent thermal and photochemical stabilities in both solution and solid states, leading to their potential use as the molecular unit for designing a new self-assembled organic photocatalyst.[181,182] One representative example involves the selection of (5,10,15,20-tetrakis(4-(7-*tert*-butyl)pyrene-2-yl) phenyl)porphyrinato iron(III) chloride (FeBPPy) as a building block. Masaoka and his colleagues[172] reported an iron-complex-based supramolecular framework catalyst (FC1), constructed through the self-assembly of FeBPPy (Fig. 9b). The photocatalytic functionality of FC1 derives from four key features: (i) the iron porphyrin complex, which serves as the catalytic center; (ii) pyrene-based substituents, which function both as light-harvesting units and as sites for noncovalent interactions; (iii) a crystalline porous framework that facilitates CO_2 accumulation; and (iv) efficient intramolecular electron transfer between the pyrene moiety and the iron porphyrin framework. Benefiting from the synergistic effects of these features, FC1 exhibits high photocatalytic activity for CO_2 reduction, achieving a record-high CO production rate of 29.1 mmol g^{-1} h^{-1} with 99.9% selectivity. Importantly, FC1 exhibited sustained photocatalytic activity over 96 hours, demonstrating its robustness and long-term operational stability. In summary, a key design strategy for achieving robust and high-performance photocatalysts lies in the use of supramolecular frameworks composed of iron porphyrin complexes bearing pyrene moieties at the meso positions.

Diareno-fused ullazine unit. Starting from the ullazine core, Dumele *et al.*[175] developed two diareno-fused chromophore

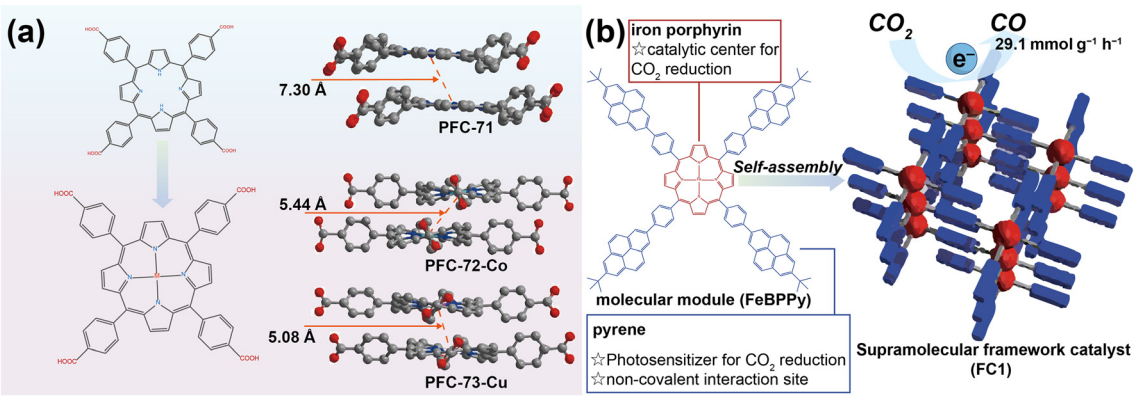

Fig. 9 (a) Schematic representation of the construction of PFC-71, PFC-72-Co, and PFC-73-Cu. Adapted with permission.[174] Copyright 2021, Wiley-VCH. (b) Structure and features of the catalyst module (FeBPPy) and the strategy to construct a supramolecular framework catalyst. Adapted with permission.[172] Copyright 2023, American Chemical Society.

amphiphiles (1 and 2) through a series of structural modifications: (i) introduction of a monoimide unit bearing a carboxylic acid headgroup *via* a five-carbon linker, enabling water solubility and inducing a dipole moment in the π-system; (ii) lateral π-extension of the ullazine core to enhance visible-light absorption; and (iii) incorporation of an *n*-pentyl tail to improve synthetic solubility and promote hydrophobic self-assembly. The resulting π-stacked supramolecular fibers efficiently sensitize dicobalt catalysts for CO_2 photoreduction to CO and CH_4 under visible light. In mixed aqueous–organic media (CH_3CN/H_2O, 4 : 1), these organic sensitizers exhibited catalytic performance comparable to precious-metal-based complexes. Remarkably, under fully aqueous conditions, their turnover numbers for CO and CH_4 production surpassed those of $Ru(phen)_3(PF_6)_2$-sensitized analogues, maintaining activity over 6 days. The combined strategy of rationally designing self-assembling chromophores to create functional soft materials will offer new insights into developing highly stable and efficient supramolecular photocatalysts.

4.2 Cooperative effects of noncovalent interactions

As previously discussed, the incorporation of multiple noncovalent interactions is critical for stabilizing π-conjugated supramolecular structures.[153,183] By reinforcing intermolecular interactions, multiple noncovalent interactions not only enhance framework stability but also enable the formation of precisely defined nanostructures with functional properties.[184] In this context, hierarchical self-assembly offers a promising bottom-up strategy to create a precisely controlled artificial photocatalytic system with high stability and efficiency. Yu *et al.*[171] reported a highly stable and efficient artificial spherical chromatophore nanomicelle system, self-assembled from Zn porphyrin amphiphiles (Fig. 10a). To achieve high surface area, multi-segment porphyrin-based amphiphiles (ZnMSA1–4) were designed to form uniform spherical nanomicelles in water without the need for any pre-treatment. Multiple hydrogen bonds positioned on both sides of the aromatic amide oligomer linkers were specifically introduced to strengthen intermolecular interactions among ZnMSA1–4 units. This design enabled the formation of highly uniform nanomicelles (Nalg-1–4) with large surface areas and exceptional structural stability. The hierarchical self-assembly of ring-like subunits within the spherical nanomicelles produced a spherical antenna effect, which facilitated the photocatalytic process. Under visible-light irradiation at ambient temperature and pressure, the nanomicelle system achieved selective photocatalytic conversion of CO_2 to CH_4 in water, with a turnover number (TON) exceeding 6600 and a selectivity of 89% over a continuous reaction period of 30 days (Fig. 10b–d).

In addition, the biological G-quadruplex moiety serves as a rigid hydrogen-bonded scaffold, ideal for designing various supramolecular assemblies, owing to its eight Hoogsteen hydrogen bonds formed among four guanine units. The planar structure of G-quadruplexes favors π–π stacking interactions, further stabilizing the hydrogen-bonded assemblies. Therefore, Jiang and colleagues[156] designed a robust 2,2′-bipyridine (bpy)-derived biological HOF (HOF-25) (Fig. 10e). The exceptional stability of HOF-25 arises from the synergistic effect of G-quadruplex hydrogen bonding and interlayer π–π interactions, imparting permanent porosity to the framework. Moreover, HOF-25 can react with $Re(CO)_5Cl$ to yield the post-functionalized framework HOF-25-Re. The stable and recyclable HOF-25-Re heterogeneous catalyst efficiently promotes the visible-light-driven photoreduction of CO_2, achieving a high CO production rate of 1448 μmol g^{-1} h^{-1} and a consistently high CO selectivity of 93% over three catalytic cycles. Upon deactivation, the photocatalytic performance of HOF-25-Re can be restored through a two-step regeneration process involving recrystallization followed by post-modification.

4.3 Assembly strategies

Although the dynamic nature of organic supramolecular systems is an attractive feature, the spontaneous assembly process often involves multiple competing pathways, including transformations between states *via* successive noncovalent bond-making and -breaking events. This pathway complexity diminishes facile access to the desired supramolecular product.[185,186] To overcome this limitation, a variety of assembly strategies have been developed to enable precise control over the self-assembly process, thereby facilitating the construction of optimized self-assembled functional materials.

For example, boron–nitrogen-embedded polycyclic aromatic hydrocarbons (BN-PAHs) have attracted considerable attention as novel π-conjugated systems due to their advantageous optoelectronic properties. However, the construction of long-range ordered supramolecular assemblies based on BN-PAHs remained rare, mainly owing to the difficulty of simultaneously coordinating multiple noncovalent interactions and the intrinsic rigidity of BN-PAHs, which hindered precise control over self-assembly behavior. To address this, Zhang *et al.*[187] reported a hierarchical assembly strategy that exploited the synergistic effects of cation-π and C–H···π interactions to enable the controlled organization of BN-PAHs (Fig. 11a–d). Under solvent-tuned conditions, 1D supramolecular assemblies were initially formed *via* cation–π interactions between the BN-PAH units. These 1D assemblies subsequently fused into 2D layered architectures through directional C–H···π interactions, allowing precise modulation of the structural transformation from 1D to 2D. The resulting 2D-BNSA structures featured precisely defined layered morphologies with a distinctive combination of rigidity and flexibility. This configuration facilitated effective dispersion and anchoring of nanocatalysts, enhancing charge separation and transport, and ultimately promoted photocatalytic CO_2 reduction. Notably, CdSe@2D-BNSA achieved a CH_4 evolution rate of 938.7 μmol g^{-1} h^{-1}, demonstrating its high efficiency in CO_2-to-CH_4 conversion.

Similarly, Zhang *et al.*[188] developed a self-adjusted aromatic cation-π binding strategy to guide the self-assembly of charged π-electronic molecules. This approach overcomes the intrinsic electrostatic repulsion between similarly charged π-systems and enables precise control over supramolecular polymorph-

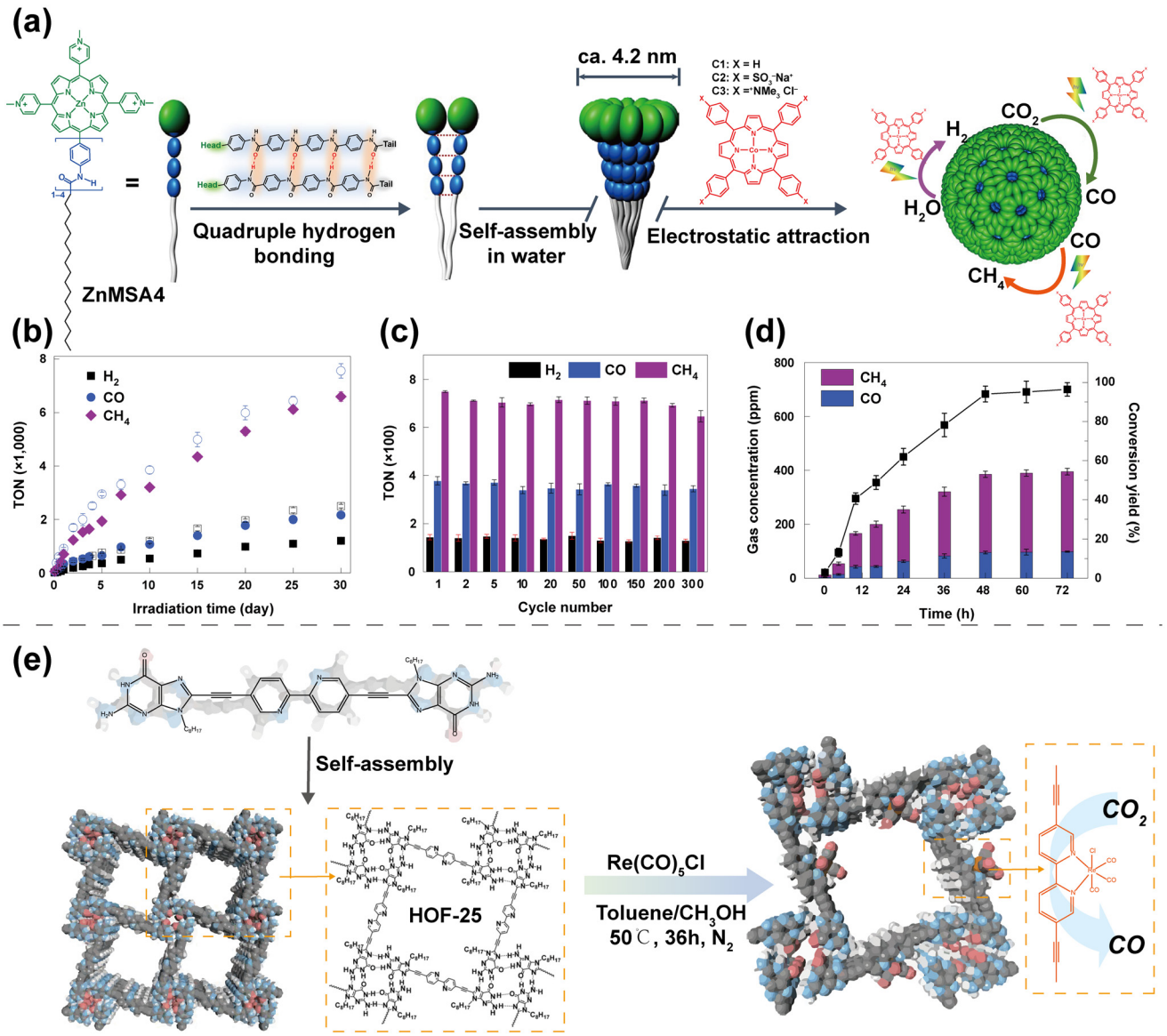

Fig. 10 (a) Formation of the quadruple hydrogen-bond enhanced nanomicelle (Nalg-4) from a self-assembling zinc porphyrin amphiphile (ZnMSA4) in water and photocatalytic H_2 production and CO_2 reduction processes over the cobalt catalyst (C2). (b) The performance of photocatalytic H_2 production and CO_2 reduction with visible-light-irradiation times up to 30 days. (c) Photocatalytic H_2 production and CO_2 reduction by Nalg-4 under visible-light irradiation with different cycling times which was recovered from centrifugation (24 h per cycle, C2 = 2 μM, [Zn] = 0.2 mM). (d) Photocatalytic CO_2 reduction from atmospheric CO_2 (~410 ppm) of a Nalg-4 solution ([Zn] = 0.2 mM) with 2 μM C2 and 20 mM TEA·HCl (with 5% TEA) under visible light. Adapted with permission.[171] Copyright 2023, Springer Nature. (e) A proposed structure of HOF-25-Re for carbon dioxide reduction [octyl chains on the guanine unit are not shown in these structures. C: grey; N: cyan; O: red; and H: white]. Adapted with permission.[156] Copyright 2021, Wiley-VCH.

ism. Strong interactions between pyridinium and benzene units promote the antiparallel head-to-tail stacking of styrylpyridinium derivatives, leading to the formation of positively charged columnar structures. These columns are further regulated by a self-adjustment process involving specific rotational dynamics around the column axis, which drives a transition from alternate overlapping to helical stacking. This versatility results in thermodynamically controlled columnar polymorphism, including alternately stacked columnar crystals, hexagonal columnar crystals, hexagonal columnar liquid crystals, and micellar cubic liquid crystals. In addition to stabilizing the columnar packing of charged π-units, the aromatic cation–π interactions facilitate charge transfer, endowing the assemblies with intrinsic photocatalytic activity for CO_2 reduction. The photoreduction performance was closely correlated with the polymorphic columnar structures. Among them, helically stacked long-column assemblies exhibited the highest activity, achieving a CO evolution rate of 82.5 μmol g^{-1} h^{-1}.

In addition, Fang *et al.*[189] reported three Zn^{2+}-based metallo-supramolecular assemblies constructed *via* coordi-

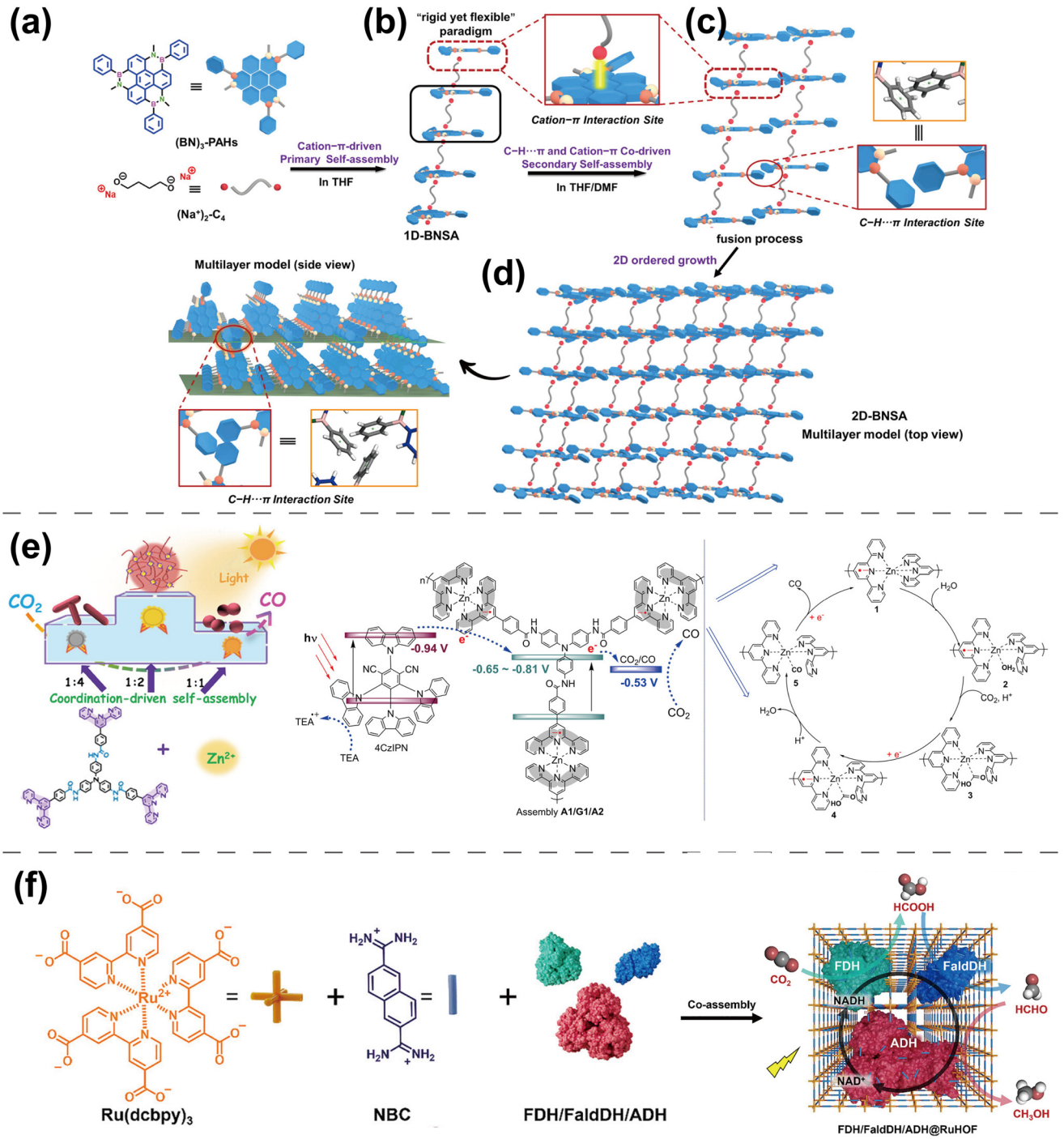

Fig. 11 (a) Chemical and mode structures of two monomers $(BN)_3$-PAHs and $(Na^+)_2$-C_4. (b) Cation–π interactions propel the formation of 1D-BNSA with a "rigid yet flexible" assembly paradigm. (c) Diagram of the fusion process of 1D-BNSA driven by synergistic C–H···π and cation–π interactions. (d) The ultimate multilayer hierarchical architecture of 2D-BNSA. Reproduced with permission.[187] Copyright 2024, American Chemical Society. (e) Proposed probable mechanism of photocatalytic CO_2 reduction using assemblies **A1**, **A2**, and **G1** with the assistance of the photosensitizer 4CzIPN and sacrificial electron donor TEA. Reproduced with permission.[189] Copyright 2023, American Chemical Society. (f) Schematic illustration of the *in situ* co-assembly of FDH, FaldDH, and ADH with precursors of photoactive HOFs to construct a photo-enzymatic cascade system, FDH/FaldDH/ADH@RuHOF, for NADH-mediated CO_2 cascade reduction to produce methanol. Reproduced with permission.[190] Copyright 2025, Wiley-VCH.

nation-driven self-assembly of a flexible tris(terpyridine) ligand (N3tpy), guided by Zn^{2+}–terpyridine coordination, hydrogen bonding, and π–π stacking interactions (Fig. 11e). Varying the metal-to-ligand ratio yielded distinct morphologies: spherical particles (A1), microrods (A2), and a fibrous gel (G1). Among them, G1 exhibited the highest CO production rate (6.3 mmol

g^{-1} h^{-1}) with 94.7% selectivity. The fibrous gel structure of G1, featuring both homogeneous and heterogeneous characteristics, is considered to facilitate electron transfer between G1 and the photosensitizer 4CzIPN. The permeable network allows 4CzIPN to diffuse efficiently into the gel matrix, unlike the more compact structures of A1 and A2.

Recently, Tang *et al.*[190] reported a multiple-enzyme integrated HOF system for cascade photocatalytic CO_2-to-methanol conversion in water (Fig. 11f). Charge-assisted hydrogen bonding between carboxylate and amidinium monomers in aqueous media directed the formation of HOF microcrystals under ambient conditions, providing a mild and biocompatible platform for the simultaneous encapsulation of enzymes. Incorporation of formate dehydrogenase (FDH), formaldehyde dehydrogenase (FaldDH), and alcohol dehydrogenase (ADH) into a RuHOF afforded a ternary cascade catalyst that enabled sustained CO_2-to-methanol conversion, producing 2.2 mM methanol with an apparent quantum efficiency of 5.5 percent (92 μM h^{-1}) over 24 hours. The integrated system retained 85 percent of its activity after five cycles, indicating the stabilizing effect of the HOF matrix on enzyme functionality. The enhanced performance was attributed to substrate and coenzyme enrichment near active sites, and the spatial confinement of the enzymes within the framework, which facilitated efficient substrate channeling and minimized diffusional losses.

5 Outlook

Heterogeneous organic photocatalysts based on π-conjugated monomers have consistently attracted attention, offering an increasingly important platform for CO_2 photoreduction due to their intrinsic properties such as structural designability, abundant reserves of constituent elements, tunable optoelectronic properties, and low cost. Precise structural design of heterogeneous organic photocatalysts involves the integration of the following mechanistic aspects: (i) extended π-conjugation to enhance light-harvesting ability and the incorporation of complementary light absorbing materials to cover a broad solar spectrum; (ii) sufficient redox potential to drive the CO_2 photoreduction reaction; (iii) periodically ordered (highly crystalline) structures to ensure uniform distribution of building blocks/functional units, and establish continuous, low-loss pathways for the efficient transport of photogenerated charge carriers; (iv) multiple accessible active sites for CO_2 adsorption and activation, enabling high reduction efficiency and product selectivity; and (v) abundant high-quality heterointerfaces to promote interfacial charge transfer. Despite considerable efforts and substantial progress in the development of these materials, fully unlocking their photocatalytic efficiency and product selectivity remains challenging. This difficulty primarily stems from the complexity of integrating all desired properties into a single, well-functioning system. Based on recent advances, we highlight the following outstanding challenges and feasible research directions:

(1) Limited diversity of π-conjugated building blocks. The current range of π-conjugated monomers with appropriate redox potentials, light-harvesting capabilities, and catalytic functionalities remains narrow, limiting the structural and functional tunability of heterogeneous organic photocatalysts. Expanding the monomer library through molecular engineering and the development of new synthetic methodologies are therefore essential. Recent advances in materials informatics, particularly AI-assisted high-throughput screening and machine learning, offer powerful tools to accelerate the identification of π-conjugated monomers with desirable optoelectronic and catalytic properties by establishing structure–property relationships.

(2) Interfacial instability and limited characterization in hybrid systems. Metallized heterogeneous organic photocatalysts and hybrid systems—such as those involving heterojunctions or cocatalyst deposition—often suffer from metal ion leaching and component separation. In addition, buried or disordered interfaces hinder detailed structural characterization, leaving the nature of interfacial architecture and its impact on photocatalytic performance poorly understood. Advancing interfacial engineering remains essential to improve the stability and efficiency of these systems.

(3) Limited mechanistic understanding of dynamic reaction processes. The dynamic evolution of catalysts and intermediate species under operating conditions is poorly understood, limiting the ability to optimize reaction pathways and active-site environments. It remains worthwhile to explore and develop advanced *in situ* characterization techniques capable of capturing the dynamic evolution of catalysts and detecting intermediate states of the reaction process in real time, thereby elucidating the reaction mechanism and the structure–property relationship. Complementarily, the integration of big data and ML enables efficient analysis. Advancements in physical characterization and supercomputers contribute to the perfection of big data storage. Based on these data, ML can simulate the entire reaction process and predict the dynamic evolution of the CO_2 reduction reaction, inferring the reaction mechanism from theoretical analysis. The combined application of *in situ* studies and ML represents a promising research direction, with the potential to significantly enhance the efficiency and depth of future investigations into CO_2 photoreduction.

(4) Insufficient assembly and processability for device-level applications. Many promising photocatalysts lack scalable processing strategies, hindering their integration into artificial photosynthetic systems with sustained operational stability. Future efforts should focus on developing assembly methods that preserve intrinsic optoelectronic properties and catalytic performance.

(5) The properties of organic polymers are closely linked to their crystallinity, highlighting the need for efficient and reproducible methods to construct well-ordered structures for reliable structure–property evaluation and performance optimization. While morphological control has been widely employed to improve the performance of various crystalline

materials, most organic polymers are formed through strong covalent linkages, which limit reversibility and present a fundamental trade-off between the polymerization rate and structural order. This challenge is particularly evident in the synthesis of large, high-quality single crystals. Therefore, the development of polymerization strategies that enable the rapid growth of highly crystalline or single-crystalline organic polymers is essential for both fundamental studies and device-level applications.

Addressing these challenges requires a synergistic approach spanning synthetic chemistry, interfacial physics, device engineering, and computational science. Progress along these directions will accelerate the rational development of efficient and selective heterogeneous organic photocatalysts for solar-driven CO_2 conversion.

Author contributions

All authors contributed in writing the original draft and reviewing and editing the manuscript.

Conflicts of interest

There are no conflicts to declare.

Data availability

No primary research results, software or code have been included and no new data were generated or analysed as part of this review. All data could be found in the related references cited in the manuscript.

Acknowledgements

This work was supported by the National Natural Science Foundation of China (12205126 and 21806181), Fundamental Research Funds for the Central Universities (2024ZKPYHH01), and the Fundamental Research Funds for the Central Universities (Ph.D. Top Innovative Talents Fund of CUMTB) (BBJ2025067).

References

1 T. Huang, J. Han, Z. Li, Y. Hong, X. Gu, Y. Wu, Y. Zhang and S. Liu, *Angew. Chem., Int. Ed.*, 2025, **64**, e202500269.
2 Y.-N. Jing, H.-X. Wang, C. Wang, C. Ye, C.-H. Tung and L.-Z. Wu, *J. Am. Chem. Soc.*, 2025, **147**, 15942–15946.
3 H. Su, H. Yin, W. Orbell, Y. Li, G. Wang, Y. Wang, K. Mori, Z. Chen, H. Li, H. Yamashita, *et al.*, *Angew. Chem., Int. Ed.*, 2025, **64**, e202425446.
4 Q. Xu, J. Han, F. Tian, X. Zhao, J. Rong, J. Zhang, P. She, J.-S. Qin and H. Rao, *J. Am. Chem. Soc.*, 2025, **147**, 10587–10597.
5 A. Hayat, M. Sohail, A. G. Al-Sehemi, N. A. Alghamdi, T. Taha, H. S. AlSalem, A. M. Alenad, M. A. Amin, A. Palamanit, C. Liu, *et al.*, *Int. J. Hydrogen Energy*, 2022, **47**, 14280–14293.
6 A. Hayat, M. Sohail, T. Taha, A. M. Alenad, A. Irfan, N. Shaishta, A. Hayat, S. K. B. Mane and W. U. Khan, *CrystEngComm*, 2021, **23**, 4963–4974.
7 T. Hisatomi, T. Yamada, H. Nishiyama, T. Takata and K. Domen, *Nat. Rev. Mater.*, 2025, **10**, 769–782.
8 X. Chang, T. Wang and J. Gong, *Energy Environ. Sci.*, 2016, **9**, 2177–2196.
9 W. Tu, Y. Zhou and Z. Zou, *Adv. Mater.*, 2014, **26**, 4607–4626.
10 S. Wang, J. Wang, Y. Wang, X. Sui, S. Wu, W. Dai, Z. Zhang, Z. Ding and J. Long, *ACS Catal.*, 2024, **14**, 10760–10788.
11 L. Ding, Z.-D. Yu, X.-Y. Wang, Z.-F. Yao, Y. Lu, C.-Y. Yang, J.-Y. Wang and J. Pei, *Chem. Rev.*, 2023, **123**, 7421–7497.
12 A. Hayat, S. Raza, M. A. Amin, Z. Ajmal, M. M. Alghamdi, A. A. El-Zahhar, H. Ali, D. Ghernaout, Y. Al-Hadeethi, M. Sohail, *et al.*, *Mater. Sci. Eng., R*, 2024, **157**, 100771.
13 A. Hayat, M. Sohail, A. El Jery, K. M. Al-Zaydi, S. Raza, H. Ali, Y. Al-Hadeethi, T. Taha, I. U. Din, M. A. Khan, *et al.*, *Mater. Today*, 2023, **64**, 180–208.
14 A. Hayat, M. Sohail, T. A. M. Taha, A. M. Alenad, M. A. Amin, A. Hayat, A. Irfan, A. Palamanit, Y. Al-Hadeethi, S. K. B. Mane, *et al.*, *Int. J. Energy Res.*, 2022, **46**, 1882–1893.
15 S. Mohata, P. Majumder and R. Banerjee, *Chem. Soc. Rev.*, 2025, **54**, 6062–6087.
16 D. Jiang, V. G. W. Tan, Y. Gong, H. Shao, X. Mu, Z. Luo and S. He, *Chem. Rev.*, 2025, **125**, 6203–6308.
17 L. Wang, L. Liu, Y. Li, Y. Xu, W. Nie, Z. Cheng, Q. Zhou, L. Wang and Z. Fan, *Adv. Energy Mater.*, 2024, **14**, 2303346.
18 S. Wang, J. Wang, Y. Wang, X. Sui, S. Wu, W. Dai, Z. Zhang, Z. Ding and J. Long, *ACS Catal.*, 2024, **14**, 10760–10788.
19 C. Feng, M. Hu, S. Zuo, J. Luo, P. Castaño, Y. Ren, M. Rueping and H. Zhang, *Adv. Mater.*, 2025, **37**, 2411813.
20 M. Li, Z. Han, Q. Hu, W. Fan, Q. Hu, D. He, Q. Chen, X. Jiao and Y. Xie, *Chem. Soc. Rev.*, 2024, **53**, 9964–9975.
21 J. Fu, K. Jiang, X. Qiu, J. Yu and M. Liu, *Mater. Today*, 2020, **32**, 222–243.
22 W. Xie, Y. Liu, X. Zhang, H. Yan, X.-H. Liu, X. Zhang, Q. Zhao and H. Huang, *Angew. Chem.*, 2024, **136**, e202314384.
23 S. Hu, P. Qiao, X. Yi, Y. Lei, H. Hu, J. Ye and D. Wang, *Angew. Chem., Int. Ed.*, 2023, **62**, e202304585.
24 Y. He, S. Dai, J. Sheng, Q. Ren, Y. Lv, Y. Sun and F. Dong, *Proc. Natl. Acad. Sci. U. S. A.*, 2024, **121**, e2322107121.
25 R. Pan, Q. Wang, Y. Zhao, Z. Feng, Y. Xu, Z. Wang, Y. Li, X. Zhang, H. Zhang, J. Liu, *et al.*, *Sci. Adv.*, 2024, **10**, eadq2791.

26 T. Yui, A. Kan, C. Saitoh, K. Koike, T. Ibusuki and O. Ishitani, *ACS Appl. Mater. Interfaces*, 2011, **3**, 2594–2600.
27 A. Kudo and Y. Miseki, *Chem. Soc. Rev.*, 2009, **38**, 253–278.
28 D. Yang, Y. Sun, N. Feng, Y. Zhong, J. Zhou and F. Zhou, *Angew. Chem., Int. Ed.*, 2025, **64**, e202419702.
29 R. Ye, L. Ma, X. Hong, T. R. Reina, W. Luo, L. Kang, G. Feng, R. Zhang, M. Fan, R. Zhang, *et al.*, *Angew. Chem., Int. Ed.*, 2024, **63**, e202317669.
30 M. Zhou, H. Wang, R. Liu, Z. Liu, X. Xiao, W. Li, C. Gao, Z. Lu, Z. Jiang, W. Shi, *et al.*, *Angew. Chem., Int. Ed.*, 2024, **63**, e202407468.
31 E. Gong, S. Ali, C. B. Hiragond, H. S. Kim, N. S. Powar, D. Kim, H. Kim and S.-I. In, *Energy Environ. Sci.*, 2022, **15**, 880–937.
32 H.-X. Liu, W.-W. Wang, X.-P. Fu, J.-C. Liu and C.-J. Jia, *Nat. Commun.*, 2024, **15**, 9126.
33 X. Li, P. Zhang, C. Yang, Z. Wang, X. Song, T. Wang and J. Gong, *Angew. Chem.*, 2023, **135**, e202301901.
34 Z.-K. Xin, M.-Y. Huang, Y. Wang, Y.-J. Gao, Q. Guo, X.-B. Li, C.-H. Tung and L.-Z. Wu, *Angew. Chem., Int. Ed.*, 2022, **61**, e202207222.
35 S. Feng, L. Wang, B. Milián-Medina, A. J. Meixner, M. S. Kwon, S. Y. Park, R. Wannemacher and J. Gierschner, *Adv. Mater.*, 2023, **35**, 2306678.
36 Z. Sun, N. Talreja, H. Tao, J. Texter, M. Muhler, J. Strunk and J. Chen, *Angew. Chem., Int. Ed.*, 2018, **57**, 7610–7627.
37 X. Li, L. Li, G. Chen, X. Chu, X. Liu, C. Naisa, D. Pohl, M. Löffler and X. Feng, *Nat. Commun.*, 2023, **14**, 4034.
38 Y. Li, Y. Chen, Q. Wang, Y. Ye, J. Zeng and Z. Liu, *Adv. Mater.*, 2025, **37**, 2414994.
39 M. Yu, M. Li, X. Zhang, Z. Ge, E. Xu, L. Wang, B. Yin, Y. Dou, Y. Yang, X. Zhang, *et al.*, *Angew. Chem., Int. Ed.*, 2025, **64**, e202423995.
40 L. Liu, S. Wang, H. Huang, Y. Zhang and T. Ma, *Nano Energy*, 2020, **75**, 104959.
41 C. Yang, S. Liu, Y. Wang, J. Song, G. Wang, S. Wang, Z.-J. Zhao, R. Mu and J. Gong, *Angew. Chem., Int. Ed.*, 2019, **58**, 11242–11247.
42 S. Mohata, P. Majumder and R. Banerjee, *Chem. Soc. Rev.*, 2025, **54**, 6062–6087.
43 Z.-K. Xin, M.-Y. Huang, Y. Wang, Y.-J. Gao, Q. Guo, X.-B. Li, C.-H. Tung and L.-Z. Wu, *Angew. Chem., Int. Ed.*, 2022, **61**, e202207222.
44 B. B. Rath, S. Krause and B. V. Lotsch, *Adv. Funct. Mater.*, 2024, **34**, 2309060.
45 W. Gui, S. Jiang, L. Wang, C. Liu, Z. Huang, L. Wang and J. Yang, *Adv. Funct. Mater.*, 2025, 2505919.
46 Z.-B. Fang, T.-T. Liu, J. Liu, S. Jin, X.-P. Wu, X.-Q. Gong, K. Wang, Q. Yin, T.-F. Liu, R. Cao, *et al.*, *J. Am. Chem. Soc.*, 2020, **142**, 12515–12523.
47 S. Wang, J. Wang, Y. Wang, X. Sui, S. Wu, W. Dai, Z. Zhang, Z. Ding and J. Long, *ACS Catal.*, 2024, **14**, 10760–10788.
48 Y. He, Q. Lei, C. Li, Y. Han, Z. Shi and S. Feng, *Mater. Today*, 2021, **50**, 358–384.
49 J. Wang, W. Liao, Y. Tan, O. Henrotte, Y. Kang, K. Liu, J. Fu, Z. Lin, L. Chai, E. Cortes, *et al.*, *Chem. Soc. Rev.*, 2025, **54**, 6553–6596.
50 J. Zhang, B. Zhu, L. Zhang and J. Yu, *Chem. Commun.*, 2023, **59**, 688–699.
51 X. Yu, C. Li, C. Gao, X. Zhang, G. Zhang and D. Zhang, *SmartMat*, 2021, **2**, 347–366.
52 Y. Yang, J. Wang, D. Li, J. Yang, M. Fang and Z. Li, *Adv. Mater.*, 2021, **33**, 2104002.
53 A. J. Heeger, *Angew. Chem., Int. Ed.*, 2001, **40**, 2591–2611.
54 Z.-F. Yao, J.-Y. Wang and J. Pei, *Chem. Sci.*, 2021, **12**, 1193–1205.
55 Z. Jia, X. Guo, X. Yin, M. Sun, J. Qiao, X. Jiang, X. Wang, Y. Wang, Z. Dong, Z. Shi, *et al.*, *Nature*, 2025, **643**, 104–110.
56 Y. Wang, A. Vogel, M. Sachs, R. S. Sprick, L. Wilbraham, S. J. Moniz, R. Godin, M. A. Zwijnenburg, J. R. Durrant, A. I. Cooper, *et al.*, *Nat. Energy*, 2019, **4**, 746–760.
57 S. Gao, Q. Zhang, X. Su, X. Wu, X.-G. Zhang, Y. Guo, Z. Li, J. Wei, H. Wang, S. Zhang, *et al.*, *J. Am. Chem. Soc.*, 2023, **145**, 9520–9529.
58 X. Zhu, N. Yang, L.-A. Zhou, C. Tian, J. Wu, T. Wang, X. Li, X. Jiang and S. Dai, *Adv. Mater.*, 2025, **37**, 2417437.
59 D. Zhou, Q. Chen, J. Zhang, T. Wang and Z.-Q. Liu, *Angew. Chem.*, 2025, **137**, e202500329.
60 S. Wang, X. Hai, X. Ding, S. Jin, Y. Xiang, P. Wang, B. Jiang, F. Ichihara, M. Oshikiri, X. Meng, *et al.*, *Nat. Commun.*, 2020, **11**, 1149.
61 J. Huang, S. Hu, X. Yuan, Z. Xiang, M. Huang, K. Wan, J. Piao, Z. Fu and Z. Liang, *Angew. Chem., Int. Ed.*, 2021, **60**, 20921–20925.
62 C. Wu, Z. Teng, C. Yang, F. Chen, H. B. Yang, L. Wang, H. Xu, B. Liu, G. Zheng and Q. Han, *Adv. Mater.*, 2022, **34**, 2110266.
63 R. Sun, X. Yang, X. Hu, Y. Guo, Y. Zhang, C. Shu, X. Yang, H. Gao, X. Wang, I. Hussain, *et al.*, *Angew. Chem.*, 2025, **137**, e202416350.
64 Q. Li, X. Li, M. Zheng, F. Luo, L. Zhang, B. Zhang and B. Jiang, *Adv. Funct. Mater.*, 2025, **35**, 2417279.
65 W. Zhao, D. Zhai, C. Liu, D. Zheng, H. Wu, L. Sun, Z. Li, T. Yu, W. Zhou, X. Fang, *et al.*, *Appl. Catal., B*, 2022, **300**, 120719.
66 F. Moruzzi, W. Zhang, B. Purushothaman, S. Gonzalez-Carrero, C. M. Aitchison, B. Willner, F. Ceugniet, Y. Lin, J. Kosco, H. Chen, *et al.*, *Nat. Commun.*, 2023, **14**, 3443.
67 C. Dai, L. Zhong, X. Gong, L. Zeng, C. Xue, S. Li and B. Liu, *Green Chem.*, 2019, **21**, 6606–6610.
68 C. Yang, W. Huang, L. C. da Silva, K. A. Zhang and X. Wang, *Chem. – Eur. J.*, 2018, **24**, 17454–17458.
69 H. Li, Y. Chen, Q. Niu, X. Wang, Z. Liu, J. Bi, Y. Yu and L. Li, *Chin. J. Catal.*, 2023, **49**, 152–159.
70 Q. Zhi, J. Zhou, W. Liu, L. Gong, W. Liu, H. Liu, K. Wang and J. Jiang, *Small*, 2022, **18**, 2201314.
71 C. Zhu, C. Gong, D. Cao, L.-L. Ma, D. Liu, L. Zhang, Y. Li, Y. Peng and G. Yuan, *Angew. Chem., Int. Ed.*, 2025, **64**, e202504348.

72 W. Geng, Y.-Y. Xiong, C.-X. Chen, S. Ning, Z. Xiong, S. Deng, Y. Tan, X. Song, M. Pan, M. Mayor, *et al.*, *Angew. Chem., Int. Ed.*, 2025, **64**, e202505546.
73 C. Zhu, J. Cheng, H. Lin, Z. Yang, Y. Huang, F. Lv, H. Bai and S. Wang, *J. Am. Chem. Soc.*, 2024, **146**, 24832–24841.
74 F. Meng, J. Wang, M. Chen, Z. Wang, G. Bai and X. Lan, *ACS Catal.*, 2023, **13**, 12142–12152.
75 Q. Li, J.-N. Chang, Z. Wang, M. Lu, C. Guo, M. Zhang, T.-Y. Yu, Y. Chen, S.-L. Li and Y.-Q. Lan, *J. Am. Chem. Soc.*, 2023, **145**, 23167–23175.
76 Y. He, Y. Zhao, X. Wang, Z. Liu, Y. Yu and L. Li, *Angew. Chem., Int. Ed.*, 2023, **62**, e202307160.
77 X. Chi, Z.-A. Lan, Q. Chen, X. Zhang, X. Chen, G. Zhang and X. Wang, *Angew. Chem., Int. Ed.*, 2023, **62**, e202303785.
78 Y.-Z. Cheng, W. Ji, P.-Y. Hao, X.-H. Qi, X. Wu, X.-M. Dou, X.-Y. Bian, D. Jiang, F.-T. Li, X.-F. Liu, D.-H. Yang, X. Ding and B.-H. Han, *Angew. Chem., Int. Ed.*, 2023, **62**, e202308523.
79 B. Cai, M. Axelsson, S. Zhan, M. V. Pavliuk, S. Wang, J. Li and H. Tian, *Angew. Chem., Int. Ed.*, 2023, **62**, e202312276.
80 L. Ran, Z. Li, B. Ran, J. Cao, Y. Zhao, T. Shao, Y. Song, M. K. H. Leung, L. Sun and J. Hou, *J. Am. Chem. Soc.*, 2022, **144**, 17097–17109.
81 M. Lu, M. Zhang, J. Liu, T.-Y. Yu, J.-N. Chang, L.-J. Shang, S.-L. Li and Y.-Q. Lan, *J. Am. Chem. Soc.*, 2022, **144**, 1861–1871.
82 S. Barman, A. Singh, F. A. Rahimi and T. K. Maji, *J. Am. Chem. Soc.*, 2021, **143**, 16284–16292.
83 M. Zhang, M. Lu, Z.-L. Lang, J. Liu, M. Liu, J.-N. Chang, L.-Y. Li, L.-J. Shang, M. Wang, S.-L. Li, *et al.*, *Angew. Chem.*, 2020, **132**, 6562–6568.
84 K. Lei, D. Wang, L. Ye, M. Kou, Y. Deng, Z. Ma, L. Wang and Y. Kong, *ChemSusChem*, 2020, **13**, 1725–1729.
85 Y.-N. Gong, W. Zhong, Y. Li, Y. Qiu, L. Zheng, J. Jiang and H.-L. Jiang, *J. Am. Chem. Soc.*, 2020, **142**, 16723–16731.
86 X. Chen, Q. Dang, R. Sa, L. Li, L. Li, J. Bi, Z. Zhang, J. Long, Y. Yu and Z. Zou, *Chem. Sci.*, 2020, **11**, 6915–6922.
87 W. Zhong, R. Sa, L. Li, Y. He, L. Li, J. Bi, Z. Zhuang, Y. Yu and Z. Zou, *J. Am. Chem. Soc.*, 2019, **141**, 7615–7621.
88 X. Yu, Z. Yang, B. Qiu, S. Guo, P. Yang, B. Yu, H. Zhang, Y. Zhao, X. Yang, B. Han, *et al.*, *Angew. Chem., Int. Ed.*, 2019, **58**, 632–636.
89 M. Lu, J. Liu, Q. Li, M. Zhang, M. Liu, J.-L. Wang, D.-Q. Yuan and Y.-Q. Lan, *Angew. Chem.*, 2019, **131**, 12522–12527.
90 W. Liu, X. Li, C. Wang, H. Pan, W. Liu, K. Wang, Q. Zeng, R. Wang and J. Jiang, *J. Am. Chem. Soc.*, 2019, **141**, 17431–17440.
91 X. Lan, J. Wang, L. Chen, H. Xu, T. Zhang and Y. Chen, *Chem. Sci.*, 2025, **16**, 13893–13904.
92 Q. Li, X. Li, M. Zheng, F. Luo, L. Zhang, B. Zhang and B. Jiang, *Adv. Funct. Mater.*, 2025, **35**, 2417279.
93 R. Das, R. Paul, A. Parui, A. Shrotri, C. Atzori, K. A. Lomachenko, A. K. Singh, J. Mondal and S. C. Peter, *J. Am. Chem. Soc.*, 2022, **145**, 422–435.
94 E. McQueen, N. Sakakibara, K. Kamogawa, M. A. Zwijnenburg, Y. Tamaki, O. Ishitani and R. S. Sprick, *Chem. Sci.*, 2024, **15**, 18146–18160.
95 K. Kong, H. Zhong, F. Zhang, H. Lv, X. Li and R. Wang, *Adv. Funct. Mater.*, 2025, **35**, 2417109.
96 J. M. Wang, Q. Y. Zhu, J. H. Lee, T. G. Woo, Y. X. Zhang, W.-D. Jang and T. K. Kim, *Nat. Commun.*, 2023, **14**, 3808.
97 K. Ishihara, A. Nakada, H. Suzuki, A. Yamakata, O. Tomita, A. Saeki and R. Abe, *J. Am. Chem. Soc.*, 2025, **147**, 20759–20769.
98 P. Fu, C. Chen, C. Wu, B. Meng, Q. Yue, T. Chen, W. Yin, X. Chi, X. Yu, R. Li, *et al.*, *Angew. Chem., Int. Ed.*, 2025, **64**, e202415202.
99 Q. Zhang, S. Gao, X. Zhao, H. Wang, Y. Guo, Z. Liu and J. Wang, *Chem. Sci.*, 2025, **16**, 15166–15176.
100 Z. Wang, C. Cao, L. Jiang, Z. Xing, J. Jia and G. Zhu, *Angew. Chem., Int. Ed.*, 2025, **64**, e202508924.
101 W. Zhao, J. Li, K. Li, J. Jiao, S. Liu, J. Yang, M. D. Frogley, Y. Peng, Y. Wang, H. Wang, *et al.*, *Angew. Chem., Int. Ed.*, 2025, e202510550.
102 L. Yang, Y. Peng, X. Luo, Y. Dan, J. Ye, Y. Zhou and Z. Zou, *Chem. Soc. Rev.*, 2021, **50**, 2147–2172.
103 Q. Shen, G. Song, H. Lin, H. Bai, Y. Huang, F. Lv and S. Wang, *Adv. Mater.*, 2024, **36**, 2310032.
104 X. Chang, T. Wang and J. Gong, *Energy Environ. Sci.*, 2016, **9**, 2177–2196.
105 L. Zhang, J. Liu and Y.-Q. Lan, *Acc. Chem. Res.*, 2024, **57**, 870–883.
106 Y. Tao, Q. Wang, C. Yang, Q. Wang, Z. Zhang, T. Zou, J. Qin and D. Ma, *Angew. Chem., Int. Ed.*, 2008, **47**, 8104–8107.
107 L. Wang, L. Wang, Y. Xu, G. Sun, W. Nie, L. Liu, D. Kong, Y. Pan, Y. Zhang, H. Wang, Y. Huang, Z. Liu, H. Ren, T. Wei, Y. Himeda and Z. Fan, *Adv. Mater.*, 2024, **36**, 2309376.
108 Y. Han, Y. Jin, X. Ding, X. Ma, T. Wang, H. Pan, D. Qi and J. Jiang, *Adv. Energy Mater.*, 2025, e03108.
109 L. Zhang, J. Liu and Y.-Q. Lan, *Acc. Chem. Res.*, 2024, **57**, 870–883.
110 L. Zhang, R.-H. Li, X.-X. Li, J. Liu, W. Guan, L.-Z. Dong, S.-L. Li and Y.-Q. Lan, *Proc. Natl. Acad. Sci. U. S. A.*, 2022, **119**, e2210550119.
111 L. Zhang, R.-H. Li, X.-X. Li, S. Wang, J. Liu, X.-X. Hong, L.-Z. Dong, S.-L. Li and Y.-Q. Lan, *Nat. Commun.*, 2024, **15**, 537.
112 D. Cao, C. Gong, Y. Han, C. Zhu, Y. Ma, Q. Xia, Y. Peng and G. Yuan, *Angew. Chem., Int. Ed.*, 2025, e202516908.
113 Y. Cheng, Y. Liu, Y. Liu, Y. Li, R. Wu, Y. Du, N. Askari, N. Liu, F. Qiao, C. Sun, *et al.*, *Nano Res.*, 2022, **15**, 8880–8889.
114 X. Meng, S. Wang, C. Zhang, C. Dong, R. Li, B. Li, Q. Wang and Y. Ding, *ACS Catal.*, 2022, **12**, 10115–10126.
115 Q. He, D. Ma, Y. Du, Q. Huang, J. Ji, X. Wang, H. Ji, W. Ma and J. Zhao, *Adv. Sci.*, 2025, 2503336.
116 W. Song, K. C. Chong, G. Qi, Y. Xiao, G. Chen, B. Li, Y. Tang, X. Zhang, Y. Yao, Z. Lin, *et al.*, *J. Am. Chem. Soc.*, 2024, **146**, 3303–3314.

117 L. Sun, Z. Zhang, J. Bian, F. Bai, H. Su, Z. Li, J. Xie, R. Xu, J. Sun, L. Bai, *et al.*, *Adv. Mater.*, 2023, **35**, 2300064.
118 M. I. Ahmad, Y. Liu, Y. Wang, P. Cao, H. Yu, H. Li, S. Chen and X. Quan, *Angew. Chem.*, 2025, **137**, e202419628.
119 R. Sun, Z. Zhu, N. Tian, Y. Zhang and H. Huang, *Angew. Chem., Int. Ed.*, 2024, **63**, e202408862.
120 Z. Meng, J. Zhang, H. Long, H. García, L. Zhang, B. Zhu and J. Yu, *Angew. Chem., Int. Ed.*, 2025, e202505456.
121 F. Xu, Y. He, J. Zhang, G. Liang, C. Liu and J. Yu, *Angew. Chem., Int. Ed.*, 2025, **64**, e202414672.
122 M. Liu, Y. Xu, Y. Liu, S. Shang, W. Gao, X. Wang, J. Hong, H. Xu, C. Hua, Z. You, *et al.*, *Angew. Chem., Int. Ed.*, 2025, e202505491.
123 Q.-P. Huang, C. Yang, Q. Yin, A.-A. Zhang, H.-X. Liu, L. Li, M.-M. Liu, Z.-B. Fang and T.-F. Liu, *Angew. Chem., Int. Ed.*, 2025, e202502009.
124 L. Zhang, J. Zhang, J. Yu and H. García, *Nat. Rev. Chem.*, 2025, 1–15.
125 K. Meng, J. Zhang, B. Zhu, C. Jiang, H. García and J. Yu, *Adv. Mater.*, 2025, 2505088.
126 P. Prabhu, V. Jose and J.-M. Lee, *Adv. Funct. Mater.*, 2020, **30**, 1910768.
127 Q. Zhi, J. Zhou, W. Liu, L. Gong, W. Liu, H. Liu, K. Wang and J. Jiang, *Small*, 2022, **18**, 2201314.
128 G. Zhang, X. Li, D. Chen, N. Li, Q. Xu, H. Li and J. Lu, *Adv. Funct. Mater.*, 2023, **33**, 2308553.
129 B. Ni, G. Zhang, H. Wang, Y. Min, K. Jiang and H. Li, *Angew. Chem.*, 2023, **135**, e202215574.
130 J.-Z. Jiang, S. Liu, Z. Li, M. G. Kim, H. Jang, X. Liu and L. Hou, *Adv. Energy Mater.*, 2025, **15**, 2405546.
131 L. Yao, A. M. Pütz, H. Vignolo-González and B. V. Lotsch, *J. Am. Chem. Soc.*, 2024, **146**, 9479–9492.
132 Q. Guan, L.-L. Zhou and Y.-B. Dong, *Chem. Soc. Rev.*, 2022, **51**, 6307–6416.
133 J.-W. Wang, F. Zhao, L. Velasco, M. Sauvan, D. Moonshiram, M. Salati, Z.-M. Luo, S. He, T. Jin, Y.-F. Mu, *et al.*, *Nat. Commun.*, 2024, **15**, 9779.
134 S. Yang, W. Hu, X. Zhang, P. He, B. Pattengale, C. Liu, M. Cendejas, I. Hermans, X. Zhang, J. Zhang and J. Huang, *J. Am. Chem. Soc.*, 2018, **140**, 14614–14618.
135 S. Li, C. Gao, H. Yu, Y. Wang, S. Wang, W. Ding, L. Zhang and J. Yu, *Angew. Chem., Int. Ed.*, 2024, **63**, e202409925.
136 W. Lin, F. Lin, J. Lin, Z. Xiao, D. Yuan and Y. Wang, *J. Am. Chem. Soc.*, 2024, **146**, 16229–16236.
137 Q. Zhang, S. Gao, Y. Guo, H. Wang, J. Wei, X. Su, H. Zhang, Z. Liu and J. Wang, *Nat. Commun.*, 2023, **14**, 1147.
138 M. V. Pavliuk, S. Wrede, A. Liu, A. Brnovic, S. Wang, M. Axelsson and H. Tian, *Chem. Soc. Rev.*, 2022, **51**, 6909–6935.
139 Y. Zhou, Z. Wang, L. Huang, S. Zaman, K. Lei, T. Yue, Z. Li, B. You and B. Y. Xia, *Adv. Energy Mater.*, 2021, **11**, 2003159.
140 W. Che, S. Zhao, W. J. Byun, T. Tao, J.-P. Jeon, Q. Zhao, Y. Shao, J. Li, J. Kim, J. S. Lee, *et al.*, *Adv. Mater.*, 2025, e06961.
141 Z. Sun, N. Talreja, H. Tao, J. Texter, M. Muhler, J. Strunk and J. Chen, *Angew. Chem., Int. Ed.*, 2018, **57**, 7610–7627.
142 K. Cheng, S. Kong, J. Wang, Q. Wang, S. Yuan, P.-Z. Li and Y. Zhao, *Angew. Chem., Int. Ed.*, 2025, e202504772.
143 M. Xu, Q. Zhang, S. Wei, S. Liu, M. Zhou, Y. Zhao, B. Li and Y. Xie, *Angew. Chem., Int. Ed.*, 2025, **64**, e202506072.
144 S. Karak, Y. Liu, A. B. M. Annuar and E. Reisner, *Adv. Mater.*, 2025, e13457.
145 C. Chen, Z. Sun, G. Qin, B. Wang, M. Liu, Q. Liang, X. Li, R. Pang, Y. Guo, Y. Li, *et al.*, *Adv. Mater.*, 2024, **36**, 2409797.
146 L. Sun, M. G. Campbell and M. Dincă, *Angew. Chem., Int. Ed.*, 2016, **55**, 3566–3579.
147 R. Ge, S. Yu, Y. Li, J. Huo, Y. Guo, Y. Kang, W. Li, Z. Bai, H. Liu, Y. Yamauchi, *et al.*, *Adv. Mater.*, 2025, **37**, 2503223.
148 Y. Zhuang, H. Li, S. Wang, H. Huang, X. Fu and J. Long, *Angew. Chem., Int. Ed.*, 2025, e202516199.
149 Y. Xiao, G. Ding, J. Tao, Z. Wang, Z. Chen, L. Chen, L. Shuai and G. Liao, *Nat. Commun.*, 2025, **16**, 7476.
150 C. Xu, M. Zhang, Q. Gao, T. Li, S. Wang, Y. Wang, Y. Liu, H.-Q. Peng, W. Zhang and B. Liu, *Adv. Funct. Mater.*, 2025, 2501067.
151 P. Gai, W. Yu, H. Zhao, R. Qi, F. Li, L. Liu, F. Lv and S. Wang, *Angew. Chem., Int. Ed.*, 2020, **59**, 7224–7229.
152 Q. Jiang, W. Zhan, X. Liu, L. Bai, M. Wang, Y. Xu and G. Liang, *Nat. Commun.*, 2023, **14**, 3935.
153 W. Niu, Z. Li, F. Liang, H. Zhang and X. Liu, *Angew. Chem.*, 2024, **136**, e202318434.
154 J. Chen, Q. Peng, X. Peng, H. Zhang and H. Zeng, *Chem. Rev.*, 2022, **122**, 14594–14678.
155 B. Yu, T. Meng, X. Ding, X. Liu, H. Wang, B. Chen, T. Zheng, W. Li, Q. Zeng and J. Jiang, *Angew. Chem.*, 2022, **134**, e202211482.
156 B. Yu, L. Li, S. Liu, H. Wang, H. Liu, C. Lin, C. Liu, H. Wu, W. Zhou, X. Li, *et al.*, *Angew. Chem.*, 2021, **133**, 9065–9071.
157 J. Wang, K. Liu, R. Xing and X. Yan, *Chem. Soc. Rev.*, 2016, **45**, 5589–5604.
158 X. Lin, Y. Hao, Y. Gong, P. Zhou, D. Ma, Z. Liu, Y. Sun, H. Sun, Y. Chen, S. Jia, *et al.*, *Nat. Commun.*, 2024, **15**, 5047.
159 X. Ma, Y. Zhang, C. Peng, Y. Che and J. Zhao, *Adv. Mater.*, 2015, **27**, 7746–7751.
160 S. Liu, S. Chen, J. Wang, G. Wang, P.-C. Duan, R. Zhu, Y. Jia, F. Bai and Y. Zhong, *Nano Lett.*, 2025, **25**, 4596–4604.
161 C. Wei, L. Li, Y. Zheng, L. Wang, J. Ma, M. Xu, J. Lin, L. Xie, P. Naumov, X. Ding, *et al.*, *Chem. Soc. Rev.*, 2024, **53**, 3687–3713.
162 J. Chen, H. Wei, I. D. Gridnev and W. Zhang, *Angew. Chem., Int. Ed.*, 2025, **64**, e202425589.
163 Y. Liu, L. Wang, L. Zhao, Y. Zhang, Z.-T. Li and F. Huang, *Chem. Soc. Rev.*, 2024, **53**, 1592–1623.
164 C. Ma, L. Qin, T. Zhou and J. Zhang, *Energy Environ. Sci.*, 2024, **17**, 8992–9026.
165 V. Caroprese, C. Tekin, V. Cencen, M. Mosayebi, N. Asmari, T. B. Liverpool, D. N. Woolfson, G. E. Fantner and M. M. Bastings, *Nat. Chem.*, 2025, **17**, 325–333.

166 N. Bäumer, S. Yamada, S. Ogi and S. Yamaguchi, *J. Am. Chem. Soc.*, 2025, **147**, 8300–8311.
167 S. Duan, M. Hua, C. W. Zhang, W. Hong, Y. Yan, A. Jazzar, C. Chen, P. Shi, M. Si, D. Wu, *et al.*, *Chem. Rev.*, 2025, **125**, 7918–7964.
168 S.-J. Bao, Y. Zou, H.-N. Zhang and G.-X. Jin, *Proc. Natl. Acad. Sci. U. S. A.*, 2024, **121**, e2407570121.
169 P. Jonkheijm, P. van der Schoot, A. P. Schenning and E. Meijer, *Science*, 2006, **313**, 80–83.
170 T. Yang, Y. Dong, C. Liu, J. Zhong, X. Sun, J. Zhang, X. Cao, X. Chen and Y. Zhu, *Adv. Funct. Mater.*, 2025, 2422348.
171 J. Yu, L. Huang, Q. Tang, S.-B. Yu, Q.-Y. Qi, J. Zhang, D. Ma, Y. Lei, J. Su, Y. Song, *et al.*, *Nat. Catal.*, 2023, **6**, 464–475.
172 K. Kosugi, C. Akatsuka, H. Iwami, M. Kondo and S. Masaoka, *J. Am. Chem. Soc.*, 2023, **145**, 10451–10457.
173 A.-A. Zhang, D. Si, H. Huang, L. Xie, Z.-B. Fang, T.-F. Liu and R. Cao, *Angew. Chem., Int. Ed.*, 2022, **61**, e202203955.
174 Q. Yin, E. V. Alexandrov, D.-H. Si, Q.-Q. Huang, Z.-B. Fang, Y. Zhang, A.-A. Zhang, W.-K. Qin, Y.-L. Li, T.-F. Liu, *et al.*, *Angew. Chem.*, 2022, **134**, e202115854.
175 O. Dumele, L. Đorđević, H. Sai, T. J. Cotey, M. H. Sangji, K. Sato, A. J. Dannenhoffer and S. I. Stupp, *J. Am. Chem. Soc.*, 2022, **144**, 3127–3136.
176 C. Ning, J. Yang, S. Bai, G. Chen, G. Liu, T. Shen, L. Zheng, S.-M. Xu, X. Kong, B. Liu, *et al.*, *Adv. Funct. Mater.*, 2023, **33**, 2300365.
177 Y. Chen, A. Li, Z.-H. Huang, L.-N. Wang and F. Kang, *Nanomaterials*, 2016, **6**, 51.
178 D. Jiang, V. G. W. Tan, Y. Gong, H. Shao, X. Mu, Z. Luo and S. He, *Chem. Rev.*, 2025, **125**, 6203–6308.
179 P. Shao, Z. Ren, B. Zhao, X. Wang, J. Li, J. Xie, B. Wang and X. Feng, *J. Am. Chem. Soc.*, 2025, **147**, 8769–8777.
180 H. Gu, G. Shi, L. Zhong, L. Liu, H. Zhang, C. Yang, K. Yu, C. Zhu, J. Li, S. Zhang, *et al.*, *J. Am. Chem. Soc.*, 2022, **144**, 21502–21511.
181 Z. Jiang, G. Huang, L. Sun, S. Wang and H. Chen, *Energy Fuels*, 2022, **36**, 12201–12211.
182 Y. Qin, Y. Wang, J. Lu, L. Xu and W.-Y. Wong, *Angew. Chem., Int. Ed.*, 2025, **64**, e202418269.
183 D. J. Lundberg, C. M. Brown, E. O. Bobylev, N. J. Oldenhuis, Y. S. Alfaraj, J. Zhao, I. Kevlishvili, H. J. Kulik and J. A. Johnson, *Nat. Commun.*, 2024, **15**, 3951.
184 J. Zhou, B. He, P. Huang, D. Wang, Z. Zhuang, J. Xu, C. Pan, Y. Dong, D. Wang, Y. Wang, *et al.*, *Angew. Chem., Int. Ed.*, 2025, **64**, e202418459.
185 S. Ogi, K. Sugiyasu, S. Manna, S. Samitsu and M. Takeuchi, *Nat. Chem.*, 2014, **6**, 188–195.
186 T. Bouwens, E. Bobylev, L. Antony, D. Poole III, E. Alarcón-Lladó, S. Mathew and J. Reek, *Nat. Chem.*, 2025, **17**, 1067–1075.
187 Z. Zhang, X. Hu, S. Qiu, J. Su, R. Bai, J. Zhang and W. Tian, *J. Am. Chem. Soc.*, 2024, **146**, 11328–11341.
188 Z. Zhang, B. Mu, X. Miao, L. Wang, H. Lu, Y. Ma and W. Tian, *Chem*, 2024, **10**, 1279–1294.
189 Y. Fang, T. Liu, L. Chen and D. Chao, *ACS Catal.*, 2023, **13**, 2086–2093.
190 J. Tang, Y. Lei, Q. Tang, S. Lei, Q.-Y. Qi, Z.-T. Li and J. Tian, *Angew. Chem., Int. Ed.*, 2025, e202516599.